ISSN 1726-5479

SENSORS & TRANSDUCERS

vol. 254
7/21

Frequency & Time: Measurements, Standards & Materials

International Frequency Sensor Association Publishing
IFSA

Sensors & Transducers

International Official Open Access Journal of the International Frequency Sensor Association (IFSA) Devoted to Research and Development of Sensors and Transducers

Volume 254, Issue 7, December 2021

IFSA Publishing: Barcelona • Toronto

Published by International Frequency Sensor Association (IFSA) Publishing. Printed in the USA.

Sensors & Transducers

Volume 254, Issue 7
December 2021

www.sensorsportal.com

e-ISSN 1726-5479
ISSN 2306-8515

Sensors & Transducers journal is an open access, peer review international journal published monthly by International Frequency Sensor Association (IFSA). Available in both: print and electronic (printable pdf) formats.

Sensors & Transducers Journal

Contents

Volume 254
Issue 7
December 2021

www.sensorsportal.com

ISSN 2306-8515
e-ISSN 1726-5479

Research Articles

Authors are encouraged to submit article in MS Word (doc) and Acrobat (pdf) formats
by e-mail: editor@sensorsportal.com. Please visit journal's webpage with preparation instructions:
http://www.sensorsportal.com/HTML/DIGEST/Submition.htm

International Frequency Sensor Association (IFSA).

Sensors & Transducers, Vol. 254, Issue 7, December 2021, pp. 1-9

www.sensorsportal.com

Sensors & Transducers

Published by IFSA Publishing, S. L., 2021
http://www.sensorsportal.com

Parallel, Multi-Channel Frequency & Time Measurements, with Picosecond Resolution

S. Johansson

Pendulum Instruments, Lotnicza 37, 80-297 Banino, Poland
Tel.: +48 (58) 681 89 01
E-mail: staffan.johansson@pendulum-instruments.com

Received: 27 October 2021 /Accepted: 6 December 2021 /Published: 30 December 2021

Abstract: A new approach to combine the performance of traditional Universal Frequency Counters (UFC) and high performance Time Interval Analyzers (TIA) in a single instrument in a portable benchtop format. For the first time in the industry, a UFC with all traditional timer/counter functions and full input signal dynamic range to 100 Vp-p has up to 5 parallel timestamping channels for frequency, period, time, or phase measurements. Advanced TIA functionality is included, like continuous timestamping with 7 ps resolution, acquisition speed of 20 MSa/s of complete measurement results, multi-stop Time Interval measurements, and continuous streaming of time stamped trigger events. Resolution enhancement techniques improve basic resolution up to 0.8 ps/Gate_Time for Frequency using linear regression, and up to 3.5 ps/Timestamp (Single-shot) using parallel multi-channel timestamping on a single input signal. This project was developed by Pendulum Instruments, Banino, Poland in close cooperation with the Military University of Technology, Warsaw, Poland.

Keywords: Zero dead-time, Multi-channel, Parallel timestamping, TIA, Frequency Analyzer, Resolution enhancement.

1. Introduction

Universal Frequency Counters and Time Interval Analyzers are two classes of instruments that have been around for many years, but they have had different typical characteristics. See Table 1.

Traditional Benchtop Universal Frequency Counters have been used in the past 50+ years as a standard tool on the R&D bench, as a component in test systems, as a precision frequency meter in metrology labs, and as a portable tool for field maintenance and calibration of frequency sources.

In the latest 20 years a new class of very-high resolution continuous time-stamping Time Interval Analyzers (TIA) in various board-level formats (PXI, PCI, PCIe) have emerged, intended for specialized applications, like semiconductor test, fast serial bus test, time-of-flight in mass spectrometry and photonic research, with a limited input signal range of typically <5 V.

A few projects have resulted in TIA performance also in stand-alone bench-top cabinets. For example, [1]).

The project described in this paper is the industry's first combination of a high-performance 7 ps TIA, and a full-featured Multi-Channel Universal 400 MHz / 24 GHz Frequency Counter/Analyzer.

Special resolution enhancement techniques enable an up to 12-fold improvement of frequency resolution and an up to 2-fold improvement of single-shot time resolution.

Table 1. *Typical* characteristics for traditional high-performance Universal Frequency Counters (UFC) and Time Interval Analyzers (TIA).

Item	UFC	TIA
Cabinet	Benchtop	Card or 19” card cabinet
Usage	Bench, Field, or ATE	Lab or ATE (special card cases)
Stand-alone operation	Yes	No
Computer controlled operation	Yes	Yes
Input Voltage	-50 V to +50 V	-5 V to +5 V
Suited for Sine signals	Yes	No
Suited for Pulse signals	Yes	Yes
Resolution	20-100 ps	1-20 ps
Multiple parallel inputs	No	Yes
Fast zero-dead-time timestamping	No	Yes
Multi-stop Time Interval	No	No

This article is based on the presented paper (ID: 6) at the 3rd IFSA Frequency & Time Conference (IFTC'2021), 22-24 September 2021, Palma de Mallorca, Spain, with some added contents, by the same author, [8].

1.1. Key Characteristics

The project called CNT-100 (Fig. 1) has the following performances:

- 5 parallel input channels with independent timestamping of input events, using common time scale;
- Housed in ½ 19” Benchtop cabinet;
- 7 ps resolution per timestamp;
- 20 MSa/s of data capture to internal memory;
- Wide input voltage range from 15 mVrms sine to ± 50 V pulses;
- All traditional Universal Frequency Counter/Analyzer measurements plus all common TIA measurements;
- Multi-stop Time Interval measurements;
- Frequency measurements to 24 GHz, other measurements from 0.001 Hz to 300 or 400 MHz.

The CNT-100 can display the numeric values of up to four separate inputs in parallel. Each input is color coded, see Fig. 2.

A second display view is the statistics parameter screen of all four input signal sources, showing mean value, maximum and minimum values, peak-to peak values, standard deviation, and Allan deviation. See Fig. 3.

Fig. 1. CNT-100 Multi-channel Frequency Analyzer from Pendulum Instruments.

Fig. 2. Simultaneous display of four 10 MHz input signals (Numeric frequency values plus voltage levels).

Fig. 3. Simultaneous display of four 10 MHz input frequencies (Statistics parameters).

A third display view is the timeline graphics display of the frequency values over time. Statistics parameters are shown in small text under the graph, Fig. 4.

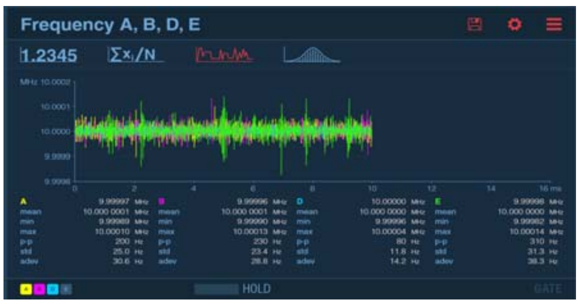

Fig. 4. Simultaneous display of four 10 MHz input frequencies (value vs. time).

The fourth and final display view of the same data set, is the graphics display of value distribution, for each input signal. Statistics parameters are shown in small text under the graph, Fig. 5.

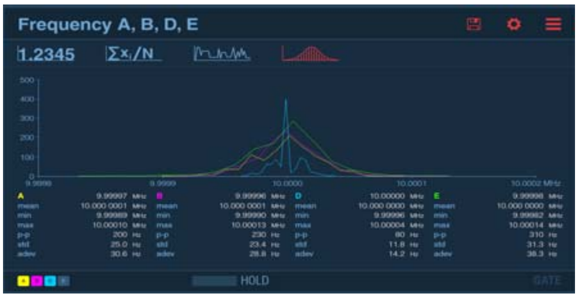

Fig. 5. Simultaneous display of four 10 MHz input frequencies (frequency distribution diagram).

2. Design

2.1. Block Diagram

A simplified block diagram of the design is shown in Fig. 6.

The **Input Signal Conditioning block**, see Fig. 7, contains all necessary analog circuitry to handle all types of input signals, whether clean or noisy, whether sine or pulse shaped, whether low or high amplitude, and to create a well-defined trigger event at the desired trigger level between -50 V and +50 V.

This blocks contains controls for:
- 50 Ω or 1 MΩ input impedance;
- AC or DC coupling;
- Attenuation ×10 or ×1;
- Trigger level settings;
- Noise reduction filters;
- Trigger sensitivity settings.

The outputs of the block are digital signals with well-defined levels, and a fast edge that coincides with the set trigger point.

Every 400 MHz input signal conditioning block is terminated with 2 independent comparators, to allow for standard pulse measurements like pulse width (trigger levels set on opposite edges at the 50 % midpoint of the slopes) or rise time (trigger levels set on rising edge at 10 % and 90 % of the slope amplitude).

2.2. Parallel Frequency Measurements

The **5-channel Digitizer block**, see Fig. 8, contains 5 fully independent time-stamping units that will timestamp incoming trigger events on up to 5 inputs in parallel. The cross-point switch, Fig. 7, selects which input channel(s) to time stamp. Any input signal can be routed to any of the 5 digitizer.

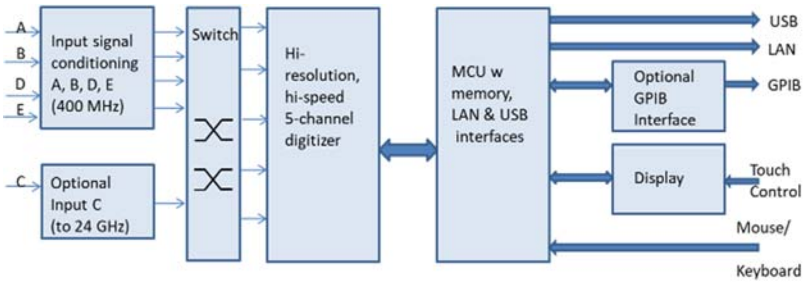

Fig. 6. Block diagram of CNT-100 (simplified).

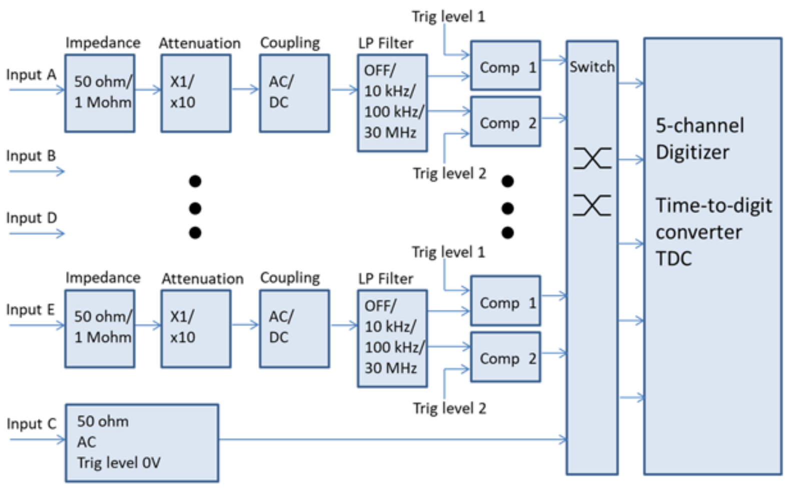

Fig. 7. Input signal conditioning.

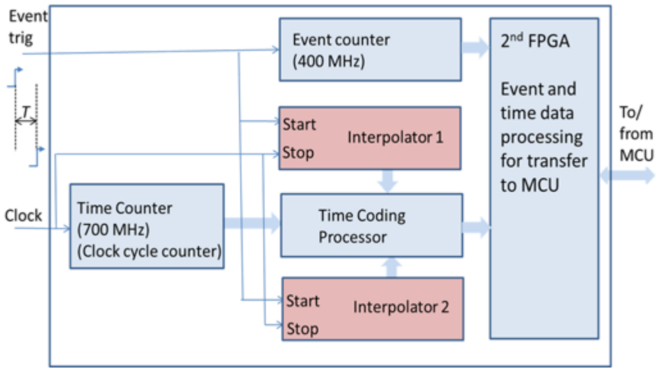

Fig. 8. Simplified block diagram of the Digitizer or Time-to-Digit-Converter block (1 channel).

The time between time stamps, commonly known as "gate time" for frequency measurements, is controlled by a pacing clock (not shown in Fig. 6) that enables capture and storage of the current number of accumulated trigger events E_i (number of input cycles), and the relative time at each capture TS_i.

The actual Gate Time is synchronized with the Input trigger Events, ensuring an exact number of input cycles between time stamps. The actual gate time can therefor differ from the set pacing time.

The Time count registers accumulates the amount of 700 MHz clock cycles, with a cycle time of 1.4 ns. This is the basic quantization resolution of the time stamp of trigger events. The interpolators improve that resolution by a factor of 200 down to 7 ps, by also measuring the fractional clock pulse, via a modified digital interpolation method, with dual Time Coding Lines as described in [1] and [2].

Fig. 9, showing the principle of a Time Coding Line, is copied from [2].

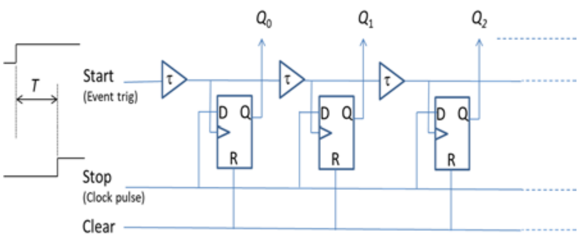

Fig. 9. Principle of the digital interpolating Time Coding Line (TLC).

The trigger event (start) triggers a chain of delay elements and D-flip-flops, with approx. 10 ps delay per delay element. The flip-flops are triggered one-by-one, and as long as the clock pulse (the stop) is in the zero state the corresponding outputs will be zero. At the clock pulse edge, the state changes from zero to one, and all subsequent flip-flops will show ones at the outputs. When all flipflops in the chain have been triggered, you could read the fractional clock pulse on the D-flipflops' outputs as a thermometer scale, all zeroes followed by all ones.

The nominal delay per delay element is 10 ps, which is also the digital interpolator's resolution step, but with quite wide variations from element to element. By using two Time Coding Lines, you could treat them as uncorrelated interpolators, thereby doubling the number of interpolation steps. The effective interpolator resolution by using dual Time Coding Lines is 7 ps.

Since the spread in the delay elements when implemented in an FPGA is wide, this interpolator design needs to be carefully calibrated before use. The CNT-100 uses the calibration principle of applying a multitude of asynchronous pulse edges to the inputs, with a random distribution within a clock pulse period, to define the transfer function, see [2].

All measurements are back-to-back, or gap-free, since the trigger event that marks the stop of one gate time, automatically is the start of the following gate time. See Fig. 10. The pacing clock has a maximum speed of 20 MHz, which means that the minimum gate time is 50 ns.

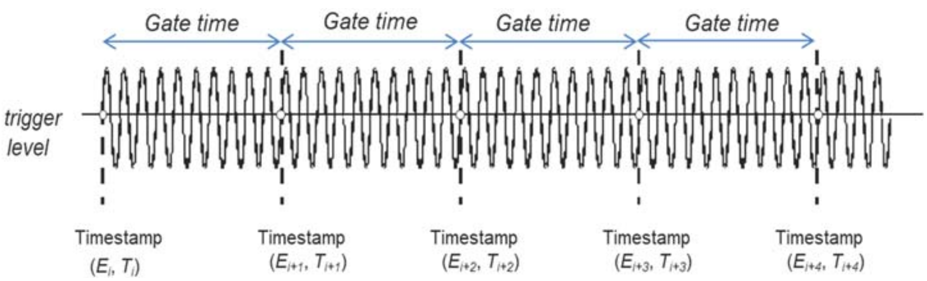

Fig. 10. Continuous zero-dead-time, gap-free, frequency measurement.

The Event data (E), with zero uncertainty (an exact number of input cycles) and Time Stamp data (TS), with 7 ps uncertainty, are transferred to the MCU which calculates frequency on-the-fly for each Gate Time period as:

$$Freq(i, i-1) = \frac{E_i - E_{i-1}}{TS_i - TS_{i-1}} \tag{1}$$

2.3. HW Configurations for Various Measurements

The CNT-100 internal HW configuration can be re-programmed to handle various types of measurement functions, either involving multiple independent parallel one-input-signal measurements, like 4x Frequency/Period, or four-input-signal inter-dependent measurements like Time Interval with one common start event and three stop events.

The basic configuration is for Frequency and Period Average, where each digitizer is connected to one of four input signals. See Fig. 11.

The comparators in the input signal conditioning stage are set to 50 % of the input signal amplitude with a positive trigger slope setting. The frequency is calculated as in Eq. (1), and the average period is calculated as the reciprocal value; $Freq^{-1}$.

The same configuration is also used for single Period measurements >50 ns.

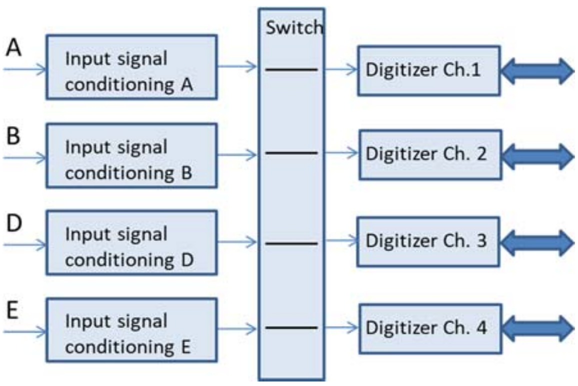

Fig. 11. Configuration for Frequency and Period Average.

For short single-shot periods from 2.5 to 50 ns, another architecture is used. The input signal is routed to two digitizers, one that timestamps the start and the other that timestamps the stop of the period. One or two input signals could be measured in parallel. See Fig. 12.

To make sure that the two digitizers are not timestamping the same trigger event, the start edge is enabling the stop edge, as shown in Fig. 12.

The comparators in the input signal conditioning stage are set to 50 % of the input signal amplitude with a positive trigger slope setting. The single period is calculated as the difference of Timestamp values between Digitizer *n* and Digitizer *n*-1, or

TS(Digitizer 2) – TS(Digitizer 1)
TS(Digitizer 4) – TS(Digitizer 3)

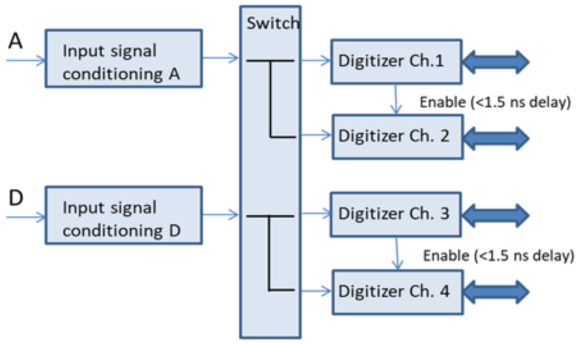

Fig. 12. Configuration for Single-shot Period measurements <50 ns.

Single-shot Time Interval measurements has yet another configuration, see Fig. 13, where input A defines the start trigger event, and inputs B, D and E defines the stop trigger events.

Each input signal is connected to its own digitizer for timestamping of the respective trigger event. To make sure that the input A signal defines the start, the start channel digitizer will enable timestamping of the other signals, the stop signals.

The comparators in the input signal conditioning stage can be set to any trigger level as required, with either positive or negative trigger slope setting. The three stop time intervals since the start trigger event, are calculated as:

TS(Digitizer 2) – TS(Digitizer 1)
TS(Digitizer 3) – TS(Digitizer 1)
TS(Digitizer 4) – TS(Digitizer 1)

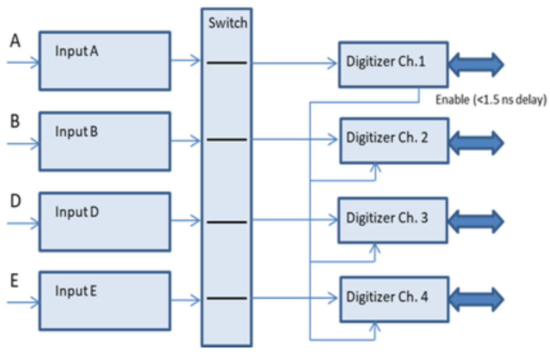

Fig. 13. Configuration for Single-shot Multi-stop Time Interval measurements.

3. Basic Measurement Uncertainty

3.1. Frequency Measurements

There are several contributing uncertainty elements in a frequency measurement. The most important being:

- Quantization error including interpolators, which is normally referred to as "resolution";
- Noise processes in the electronics, both internal and external;
- Temperature, which can cause offsets in the timebase oscillator, and the calibration of interpolators;
- Ageing of the timebase reference oscillator.

By tradition, the first two error factors are called random errors, and the last two are called systematic errors.

The *random errors* results in stochastic variations of the measured value, with the assumption that you could approximate the distribution as Gaussian. The resolution and noise trigger errors are therefore normally expressed as "rms-values".

By making N measurements (observations) and calculate the mean value you can reduce the effect of these errors with $\sqrt{N}$.

The effect of systematic errors cannot be reduced by averaging N measurements, hence the name "systematic". These factors are normally expressed as being inside a given boundary. For example: temperature effect on a timebase oscillator is ±1E-10 (0 to +50 degrees), or ageing per month is <5E-11.

The resolution and noise trigger are Type A components, and the Timebase oscillator offset due to temperature and ageing are Type B components according to [4].

The combined measurement uncertainty U of the relative random uncertainty (u_{rnd}) and the relative systematic uncertainty (u_{syst}) is shown in Eq. (2), under the assumption that the effect of all contributing error factors are uncorrelated [4], p. 19 eq. 11). If they are correlated, the expression is more complex ([4], p. 21).

$$U = \sqrt{u_{rnd}^2 + u_{syst}^2} \tag{2}$$

Let's assume we use a "perfect" external timebase oscillator, at a precisely controlled temperature, as frequency reference, e.g. a Cs oscillator or a Hydrogen Maser. Then we can neglect the influence of the timebase used on the measurement uncertainty, and only focus on the random uncertainty.

The relative random uncertainty (u_{rnd}) rms of a basic frequency measurement involving two timestamps (start and stop of Gate Time), is found in Eq. (3) below.

$$u_{rnd} = \frac{\sqrt{2 * TS_{res}^2 + 2 * noise\_trig\_err^2}}{Gate\_Time} \tag{3}$$

The noise trigger error contribution (in seconds rms) is caused by external and internal noise, and calculated as:

$$\frac{\sqrt{(ext.noise\ voltage)^2 + (int.noise\ voltage)^2}}{input\ signal\ slewrate\ (\frac{V}{s}) at\ trig.point} \tag{4}$$

With a specified internal noise of <500 µVrms, and typical internal noise of 200 µVrms, the typical noise trigger error contribution is neglectable for pulses with slew rate >0.1 V/ns, or high frequency sinewaves >20 MHz @1Vrms, where both cases give <2 ps rms noise error contribution. But it could be quite substantial for low frequency, and/or low level, sine waves, with consequently low slew rates.

Conclusion: For high-slew rate input signals, and a very high-performance Cesium clock or Hydrogen Maser (timebase error 2E-12 or less) used as external timebase reference at a constant ambient temperature, the relative uncertainty for frequency measurements is solely dependent on the Timestamp resolution.

With a TS_{res} of 7 ps rms in CNT-100, the relative frequency measurement uncertainty (Eq. (3), or relative frequency error, is:

$$u_{rnd} = \frac{10\ ps}{Gate\_Time} \tag{5}$$

Note that the *relative* error, Δf/f, is independent of actual frequency, as long as a high slew rate input signal is applied.

The displayed resolution will normally be 11-12 result digits, for a 1 s gate time for a basic frequency measurement, with one Timestamp at the Gate time start event, and one Timestamp at the Gate time stop event.

3.2. Frequency Resolution Improvement via Regression Line Fitting

However, this basic resolution can be significantly improved by taking 1000 intermediate time stamp values during the gate time, instead of just two timestamps at the start and stop of the gate time and fitting all points $TS[E(k)]$ to a regression line, using least squares method. The input data is the continuous phase change vs. time during the gate time.

The slope of the regression line is a more accurate estimate of average period (=frequency^{-1}), than the basic 2-timestamp method. The uncertainty is not only determined by the two timestamps at the start and stop of the gate time, but also on the 1000 timestamps during the measurement.

This resolution enhancement technique in a counter is described in detail in [3] as the first industrial implementation in a commercial counter, and in [6] with a solid statistics analysis of this so called "Ω-type" of frequency counting technique.

The relative random uncertainty (resolution), assuming neglectable noise trigger errors, is enhanced to:

$$u_{rnd} = \frac{\sqrt{12} \cdot TS_{res}}{Gate\_Time \cdot \sqrt{N-2}} \tag{6}$$

See [3] and [6].

In CNT-100, N is set to 1000, which means an improvement of resolution, compared to the 2-timestamp frequency measurement of $\frac{\sqrt{6}}{\sqrt{998}}$ or approx. 12.5 times. If we still neglect the noise trigger error, the resolution for frequency measurements on fast pulses is improved to:

$$u_{rnd} = \frac{0.8\,ps}{Gate\_Time} \tag{7}$$

Note that these enhanced resolution frequency results cannot be used as input values for standard Allan Variance (AVAR) calculation. Instead, they can be used for Parabolic Variance (PVAR) calculation, see [7].

This resolution enhancement mode can be applied for set gate times from 80 µs (= 80 ns minimum Sample Interval * 1000 timestamps) and up.

Note that this resolution enhancement mode improves the resolution of the measuring instrument itself, but the full improvement effect on the displayed values is also dependent on the test signal. The method is based on *linear* regression, which will improve the resolution as intended on measurements of stable frequency signal sources with a white noise.

A constant and stable frequency value is represented by a straight line in the Events vs. Timestamps graph, which is the perfect signal for improvement via linear regression line fitting. In these cases, we should see the projected 12x resolution improvement.

A non-linear frequency will not be a straight line in the graph, and then the linear regression is less fitted for resolution improvement.

Examples of non-linear signals under test include for example modulated signals, frequency drifting signals, or signals subject to periodic spikes or “outliers”.

In extreme cases the calculated average frequency result could even be less accurate with the linear regression enhancement technique, for example with a strong drift during the Measurement Time MT.

A frequency source with a frequency drift, can be described as:

$$f(t) = f_0 + f_d(t), \tag{8}$$

where f_0 is the start frequency value, $f_d(t)$ is the frequency drift over time, with mean value ≠ 0 Hz.

If $f_d(t)$ has a *linear* drift with time, then $f_d(t) = d \cdot t$, where d is the frequency drift rate (Hz/s). A linear drift during the measurement would result in an accumulated phase $\phi(t)$ vs time relation that is expressed as:

$$\Phi(t) = 2\pi f_0 t + \pi d t^2 + \Phi_0 \tag{9}$$

Fig. 14, copied from [3], p. 6, shows a simulation example with an exaggerated frequency drift, according to Eq. (9). The straight line is the regression line, and the dotted line is the accumulated phase, expressed as number of accumulated signal periods (Event counts) vs. time.

The accumulated phase is a 2nd order function and should ideally be approximated with a 2nd order polynomial and not a 1st order straight line.

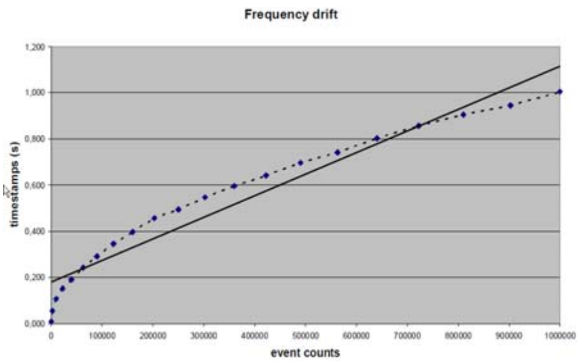

Fig. 14. A regression line can give additional error if there is a strong frequency drift.

It is obvious from the graph that the slope of the regression line is a worse representation of average frequency, compared to the true average frequency represented by the slope of a straight line from first to last timestamp during the Measurement Time MT.

3.3. Single-shot Period Resolution Improvement via Parallel Measurements

A single-shot period is the time for one individual cycle, not the average of a multiple cycles as in frequency or average period measurements.

A normal single-shot period >50 ns is measured as the difference between two consecutive timestamps in each digitizing channel. Up to 4 input signals can be measured in parallel, see Fig. 15.

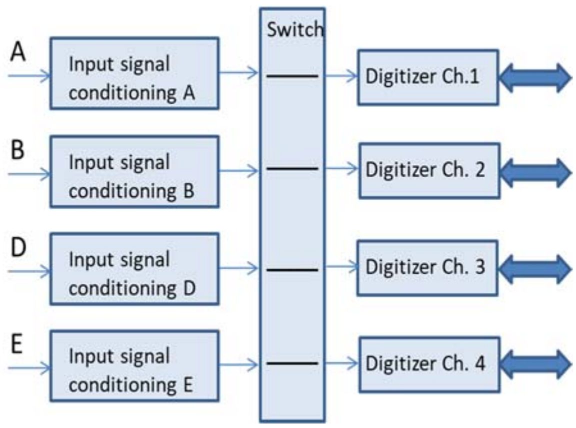

Fig. 15. Configuration for Single-shot Period measurements >50 ns.

The regression line fitting for resolution improvement is based on multiple timestamps of trigger events during the Measurement Time. It works fine for continuous Frequency and *Period Average* measurements on a stable input signal, but cannot be applied for single shot events, like a *single period* measurement.

Then you are back to the basic 10 ps per period (2 timestamps), resolution, or 7 ps per timestamp in each channel.

However, instead of timestamping the trigger events in four separate input signals in parallel, you could route one and the same input signal with a period >50 ns to five independent time digitizing channels and calculate the average value, between the start and stop trigger events in each separate channel.

This technique is described in [1]. See Fig. 16.

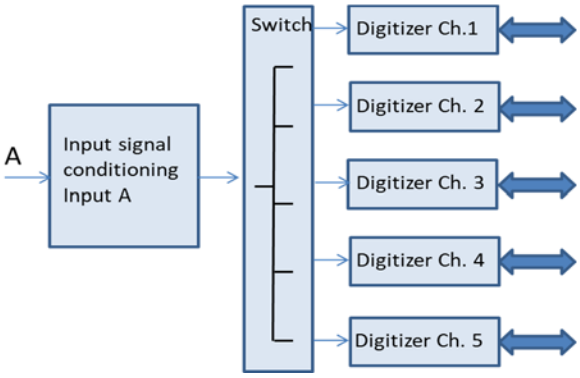

Fig. 16. Single-shot period resolution is improved up to 2 times by averaging parallel timestamping in 5 digitizers.

Note that all five digitizers are used in this special mode, as opposed to the earlier described examples involving four digitizers.

The resolution is improved approximately 2 times (square root of the number of parallel measurements minus one), and the resolution per timestamp for single periods >50 ns is improved from 7 ps to theoretically 3.5 ps.

Note that the actual improvement may be less than the theoretical value, due to the fact that the five channels are not perfectly independent and uncorrelated, which is a prerequisite for this statistical calculation.

Note that this resolution improvement is not applicable to short time intervals <50 ns, since these measurements require a basically different HW configuration, see Fig. 12.

4. Conclusion

A new combined Multi-channel Universal Frequency Counter (UFC) and Time Interval Analyzer (TIA), is presented having a 5-channel parallel continuous time stamping architecture, with a basic measurement resolution for each channel of:

10 ps/Gate_Time for frequency measurements (UFC mode), and

7 ps/Timestamp for single-shot time measurements (TIA mode).

This can be improved via resolution enhancement techniques up to (best case):

0.8 ps/Gate_Time for continuous frequency measurements (UFC mode), and

3.5 ps/Timestamp for single-shot time measurements (TIA mode), for single-period measurements.

Acknowledgements

This project was defined and developed by Pendulum Instruments in close cooperation with the *Military University of Technology, Faculty of Electronics, Warsaw, Poland (MUT).*

The high-resolution measurement kernel is designed by MUT, based on refinement of earlier MUT designs ([1] and [2]).

We would especially acknowledge the MUT team; Ryszard Szplet, Pawel Kwiatkowski, Zbigniew Jachna and Krzysztof Różyc for their dedicated contribution.

References

[1]. R. Szplet, P. Kwiatkowski, K. Różyc, Z. Jachna, T. Sondej, Picosecond-precision multichannel autonomous time and frequency counter, *Review of Scientific Instruments*, Vol. 88, Issue 12, 2017, 125101.

[2]. R. Szplet, P. Kwiatkowski, Z. Jachna, K. Różyc, A 2.9 ps equivalent resolution interpolating time counter based on multiple independent coding lines, *Measurement Science and Technology*, Vol. 24, Issue 3, 2013, 035904.

[3]. S. Johansson, New frequency counting principle improves resolution, in *Proceedings of the IEEE Int. Freq. Control Symp. Expo*, Vancouver, BC, Canada, Aug. 2005, pp. 628-635.

[4]. Guide to the expression of uncertainty in Measurement (GUM), ISO publication, 1993.

[5]. User's manual for CNT-100, *Pendulum Instruments*, document number 4031 601 10001.

[6]. Enrico Rubiola, Michel Lenczner, Pierre-Yves Bourgeois, François Vernotte, The Ω Counter, a Frequency Counter Based on the Linear Regression, *IEEE Transactions on Ultrasonics, Ferroelectrics, and Frequency Control*, Vol. 63, Issue 7, July 2016, pp. 961-969.

[7]. F. Vernotte, M. Lenczner, P.-Y. Bourgeois, E. Rubiola, The parabolic variance (PVAR): A wavelet variance based on the least-square fit, *IEEE Transactions on Ultrasonics, Ferroelectrics, and Frequency Control*, Vol. 63, Issue 4, April 2016, pp. 611-623.

[8]. S. Johansson, A new picosecond Multi-Channel combined Universal Frequency Counter & Time Interval Analyzer in a Benchtop format, in *Proceedings of the 3rd IFSA Frequency & Time Conference (IFTC'2021)*, Palma de Mallorca, Spain, 22-24 September 2021, pp. 25-29.

Sensors & Transducers, Vol. 254, Issue 7, December 2021, pp. 10-15

Sensors & Transducers

Published by IFSA Publishing, S. L., 2021
http://www.sensorsportal.com

Equivalent Phase Allocation Method Based on Frequency Measurement without Dead Zone

[1] Wenhao Zhang, [1] Miao, [1] Wei Zhou, [1] Hong Zhu, [1] Yubo Xin and [2] Zhuang Cai

[1] Xidian University, Xi'an, China
[2] Shaanxi Hua Xing Electronic Information Group Co., LTD, China
Tel.: 18394330607
E-mail: w_h_zhang@126.com, wzhou@xidian.edu.cn

Received: 25 October 2021 /Accepted: 30 November 2021 /Published: 30 December 2021

Abstract: In the field of precise time-frequency measurement and control, high resolution, time-dead zone and frequency measurement without dead zone are very important. In this paper, a frequency measurement method without dead zone is proposed, which locks the phase of the frequency signal output by the frequency synthesizer on the measured signal. By detecting the change of phase difference between the measured signal and the DDS output frequency signal, the DDS frequency control register and the phase shift control register are changed to realize the phase tracking. The frequency of the measured signals is calculated according to the phase change rule of the two signals. The experimental results in this paper show that the method achieves a measuring stability of 10^{-13}.

Keywords: Without dead zone, Frequency measurement, Phase tracking, DDS.

1. Introduction

As one of the seven international standard physical quantities, time is a component of many derived physical quantities and has the highest measurement accuracy among the current basic measurement units. In many fields such as aerospace, electric power and optical fiber communication, high precision time interval and frequency signal are needed. Precise time and frequency signal provide necessary reference signal for measurement and control. Precision time and frequency provide the necessary reference signals for measurement and control [1]. High precision time has good linearity and accuracy, which can more objectively reflect the motion law of the object. Therefore, in recent years, the world has attached great importance to the research of precision time and frequency measurement technology. At present high precision in any frequency measurement equipment, the measuring principle of many devices are dead zone of frequency measurement. For example, the 53230A frequency meter developed by Keysight has a 12-bit frequency measurement resolution, is a typical commercial frequency counter [2], but difficult to achieve without dead zone under high measuring resolution of frequency measurement, This seriously affects its application in the field of precision frequency measurement.

Because the phase information between two sampling periods is omitted in the frequency measurement method with dead zone, the measurement results cannot fully reflect the long-term frequency stability of the measured signal. When Aaron variance is used to characterize the measured results in the time domain, the stability curve changes as $1/\sqrt{\tau}$. However, when the phase ratio method is used for measurement, no phase information is omitted between the two measurements, and the stability curve of the measurement results changes with the rule of $1/\tau$. However, phase ratio is usually only used for the measurement of the same frequency standard, can not meet the needs of any frequency measurement. In this paper, a frequency measurement method without dead zone is proposed. Since no phase information is omitted in the frequency measurement method without dead zone, the measurement results can be equivalent to phase comparison, and the measurement range is large, which can measure any frequency signal between 1 and 80 MHz.

2. Frequency Stability

The indicators of the clock source mainly include accuracy and stability. Accuracy refers to the error between the real frequency of the oscillator and the nominal frequency. Generally, atomic clocks are used as clock sources in occasions that have higher requirements for frequency accuracy, and the clocks of various devices are locked on the atomic clocks through a phase-locked loop method to obtain higher accuracy. Stability refers to the ability of the frequency source to keep the frequency constant, and the Allan variance is usually used as an index to judge the stability. When studying the stability of crystal oscillators and atomic clocks, people found that the phase noise of these systems includes not only white noise, but also flicker noise. When using traditional statistical tools (such as standard deviation) to analyze this type of noise, the statistical results cannot be converged .In order to solve this problem, David Allan proposed the Allan variance in 1966. Nowadays, the Allan variance is used to characterize the frequency stability of clock sources in the time domain. In fact, not only oscillators, but any frequency source can use Allan variance to evaluate its frequency stability. Usually when using frequency data to calculate the Allan variance, the expression is:

$$\delta_y^2(\tau) = \frac{1}{2(M-1)} \sum_{i=1}^{M-1} [y_{i+1} - y_i]^2, \qquad (1)$$

where τ is the sampling time, the calculation result of the Allan variance is a series of data with τ as the abscissa, M is the number of samples, and are the frequency values of the i^{th} and $(i+1)^{th}$ measurements. Allan variance can reflect the stability of the frequency source over different sampling time lengths. If the sampling is without dead zone, that is, there is no omission between the two sampling data. The data can truly reflect the nature of the clock source, and the obtained Allan variance curve decreases with a slope of, that is, every ten times the sampling time increases, the Allan variance value also decreases by one-tenth. If the measurement method with dead zone is adopted, that is, there is no correlation or discontinuity between the data, the curve will decrease at a slope of, that is, the sampling time will increase by one hundred times, and the Allan variance will decrease by one-tenth. Phase comparison is an indirect frequency measurement method, which is generally carried out when the nominal values of the two frequency sources are the same. The phase comparison method can be used to measure the phase change relationship between the two signals. After the measurement result is converted into frequency stability, the change law of the stability curve follows. The interval frequency measurement method usually intercepts the phase change law within a period of time. The phase information between the two tests is lost, resulting in the change law of the stability curve to follow, while the frequency measurement method without interval collects all phase information. Can be equivalent to phase comparison.

For frequency measurement equipment, it is usually used to measure its own reference clock, and the Allan variance obtained is used as the noise floor of the instrument. The measurement methods proposed in this article all use this method to evaluate the noise floor.

3. Principle of Phase Tracking

In this method, the principle used is basically the same as the digital PLL, The voltage controlled oscillator is replaced by a programmable frequency synthesizer, and the PI operation is replaced by the main controller. When the PLL is locked, the frequency of the frequency synthesizer is equal to the frequency of the measured signal [3]. However, the two frequencies can not be exactly the same, but a process of dynamic balance, so the voltage of the identification sign will constantly drift, and the true frequency of the measured signal can be obtained by measuring the phase of the identification sign and its basic principle is shown in Fig. 1.

Suppose the measured signal is f_x, the frequency generated by the frequency synthesizer is f_{syn}, and the difference frequency f_{beat} of the two signals is obtained after the phase discriminator, and f_{beat} is the identification signal. Let f_{syn} frequency be slightly higher than f_x, then:

$$f_{beat} = f_{syn} - f_x \qquad (2)$$

Control f_{syn} to approach f_x so that the frequency of f_{beat} is low. The phase information of f_{beat} is transformed into voltage information, which is the phase discrimination voltage. Suppose the functional relationship between the phase of the identification signal and the phase detection voltage is:

$$\varphi = f(u) \qquad (3)$$

Use an ADC to sample at fixed dead zones. Set the sampling dead zone as Δt and the voltage of two samples as u_1 and u_2 respectively, then:

$$\Delta\varphi = f(u_2) - f(u_1) \tag{4}$$

Since the phase is the integral of frequency, the frequency of the differential frequency signal is:

$$f_{beat} = \frac{\Delta\varphi}{\Delta t} \tag{5}$$

After the frequency f_{beat} of the signal is measured, the frequency of the measured signal can be calculated by Eq. (5).

In this method, high precision program-controlled frequency synthesizer is used to approximate the measured frequency and produce the frequency as close as possible to the measured frequency. If the two frequencies are exactly the same, it can be considered that the frequency generated by the frequency synthesizer is the measured signal, but the digitally controlled frequency source will be limited by its digital quantization bit, for any measured signal, it is impossible to use the digital frequency source to produce the exact same frequency. In fact, the PLL using the analog method is not exactly the same frequency, only that the locked oscillator frequency, or its frequency after the frequency divider is very close to the reference signal frequency [4]. Its real frequency fluctuates back and forth near the reference frequency. When the locking quality is good and the VCO signal closely follows the reference signal, the stability between the two is very good and the error frequency is very small. For a good PLL, the frequency stability between the output frequency and the reference signal can be better than 10^{-15} orders of magnitude.

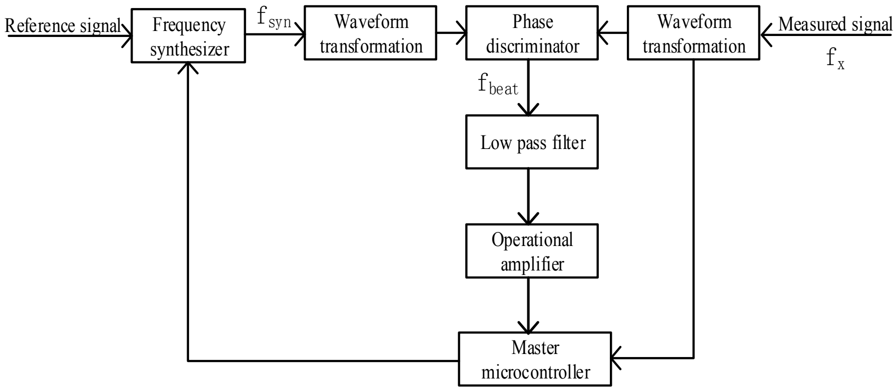

Fig. 1. Principle block diagram of frequency measurement method based on phase tracking.

4. Frequency Synthesis Method Selection

There are three commonly used frequency synthesis methods:

The first is to complete frequency synthesis directly through mixers, frequency multipliers and frequency dividers. A very common method is to extract the harmonics of a square wave or pulse signal. A method of generating a 90 MHz signal from a 10 MHz signal is as follows: the reference 10 MHz sine signal is converted into a square wave signal. The frequency spectrum component of the square wave contains odd harmonics of the fundamental frequency signal, which contains 90 MHz frequency components. Use multi-stage band-pass filters and amplifiers to extract them, and then complete the frequency multiplication. If even harmonics are needed, the reference signal can be converted into pulses. This method can be used to complete frequency synthesis with good stability. However, when this method is used in the complex frequency conversion process, there are many components, high cost, complex circuit, and difficult debugging. In this solution, the signal under test is required. The frequency produces the same frequency, and its frequency synthesis is very complicated, so this method is not suitable for this scheme.

The second method is to use a phase-locked loop and a frequency divider. Using a wide-range voltage-controlled oscillator with a flexible reference signal divider, feedback signal divider and output divider can also generate many frequencies. Suppose the frequency division number of the reference signal frequency divider is, the frequency division number of the feedback signal frequency divider is, the output of the VCO is then output through the programmable frequency divider, and the frequency division number is, then the output signal and the reference signal Functional relationship:

$$f_{out} = f_{ref} \times \frac{N_{divider}}{R_{divider} \times VCO_{divider}} \tag{6}$$

Controlling the three frequency dividers can flexibly generate many frequencies, and the noise introduced in the frequency synthesis process can be very small. But for any measured signal, it is difficult to adjust the frequency step value to be small enough, and this scheme requires the frequency generated by the frequency synthesizer and the measured signal to be as small as possible, and it is best to reach below mHz, so the phase-locked loop The method is also not suitable for this program.

The third type is Direct Digital Synthesis. DDS uses high-speed DAC to directly generate sinusoidal waveforms, which can easily generate various frequency points and complete various tasks such as frequency modulation and phase modulation. Some DDS can be prepared in advance Good digitized waveform data generates waveforms, which is very flexible and has been widely used in various fields.

The DDS chip is mainly composed of an N-bit phase accumulator, a sine look-up table storage ROM, and a DAC. Some chips also integrate a voltage-controlled oscillator and a phase-locked loop. DDS controls the DAC to generate waveforms at a certain sampling rate. The data of the DAC comes from the ROM, and the sine look-up table is stored in the ROM. In Single-Tone mode, DDS generates a single frequency without introducing any modulation signal.

At this time, the phase accumulator accumulates according to the frequency control word (FTW, Frequency Turning Word). The larger the frequency conversion word, the larger the interval between the data obtained each time, that is, the larger the phase difference, the higher the output frequency. high. Send the corresponding amplitude data to the DAC, the ROM sends the data again and again, and the DDS generates a periodic signal. The signal is of ladder type, after adding a low-pass filter to filter out the sampling frequency, a sinusoidal signal can be obtained. Some DDS also has a phase shift function, which can realize functions such as phase modulation. The output frequency of DDS is determined by the sampling clock frequency, the number of bits of the phase accumulator N, and the frequency control word. For an N-bit frequency control word, it generally corresponds to an N-bit ROM. There are points stored in the ROM, then the phase of the nth point for:

$$\varphi(n) = \frac{2\pi n}{2^N} \tag{7}$$

The frequency control word indicates the point interval between two points taken. For a certain, the phase interval between two points taken is:

$$\varDelta\varphi(n) = \frac{2\pi FTW}{2^N} \tag{8}$$

If the sampling clock frequency is, the phase sampled in one second is:

$$\varphi_{1s} = f_s * \varDelta\varphi = f_s * \frac{2\pi FTW}{2^N} \tag{9}$$

Convert it to frequency to get:

$$f_O = \frac{FTW}{2^N} f_s \tag{10}$$

The number of bits N of the phase accumulator and the sampling clock together determine the frequency resolution of the DDS.

$$f_{res} = \frac{f_s}{2^N} \tag{11}$$

The frequency resolution of DDS represents the minimum frequency difference between two different frequencies that it can output. When the frequency control word changes by 1, the frequency change of DDS is its frequency resolution. Generally, the frequency generated by DDS should not be greater than 40 % of its sampling rate. According to the Nyquist sampling theorem, the actual output frequency of DDS should not be greater than 50 % of the sampling rate. In fact, when is greater than, the output frequency of DDS is:

$$f_O = (1\text{-}\frac{FTW}{2^N}) f_s \tag{12}$$

Based on this principle of frequency synthesis, DDS can quickly jump between different frequencies, the output frequency range is very wide, from its resolution to 40 % of the sampling clock, the frequency step is also very small, and can pass The programming mode is flexibly controlled, and it has been widely used in signal receivers and radar communication systems. Because its phase and amplitude are discontinuous after all, the noise of the signal produced by DDS mainly comes from phase truncation error and amplitude quantization error. In addition, there is the nonlinearity of the DAC, which all have an impact on the technical indicators of the DDS. These factors need to be considered comprehensively in high-precision application scenarios.

The frequency synthesizer sampled in this design is the direct digital frequency synthesis chip AD9952 of Analog Devices. The frequency control word of this chip is 32 bits, the maximum sampling rate can reach 400MSPS, the chip has its own phase-locked loop, and the maximum multiplier is 20. When using a 10 MHz signal as a reference, the internal clock can reach 200 MHz. If the signal is output at 40 % of the sampling rate, a signal of up to 80 MHz can be obtained. When working at a sampling rate of 200MSPS, its frequency resolution can be better than 50 mHz. At least three IO ports are required to control the chip, which saves IO resources. During PCB layout, the occupied area is small, the structure is simple, and the cost of the chip is relatively low.

5. Experimental Results and Analysis

This section describes the experimental investigation and analysis of the results in the frequency measurement method for realizing phase tracking.

In this experiment, use the rubidium clock's 10 MHz signal as a reference signal is used to track the phase of the measured signal using a direct frequency synthesizer (DDS) [5]. First, the frequency of the measured signal was measured to the order of Hz by the gate method, and the frequency of DDS was adjusted close to the measured signal, so that the frequency difference between the two was less than

10 Hz. Then double D flip-flop is used as phase discriminator to detect DDS signal and measured signal. Then an ADC analog-to-digital converter is used to measure the signal, and the frequency of the signal is calculated according to the voltage change speed of the signal, and then the DDS frequency is adjusted closer to the frequency of the measured signal to within 50 mHz. Then enter the precision measurement, use the operational amplifier to amplify the local voltage of the identification signal, and continue to use DDS phase compensation, so that the voltage of the identification signal is always within the sampling range of the ADC. The voltage sampling and DDS phase compensation are carried out with a period of one second. The phase change speed of the detected signal is calculated using the ADC sampling value measured for two adjacent times and the phase of DDS, that is, the frequency difference between the DDS signal and the measured signal. Then, the frequency of the measured signal can be calculated according to the frequency of DDS.

When testing its performance, we using a frequency measuring instrument to test the reference signal, the result obtained is the floor noise. During self-calibration, the 10 MHz signal is used as the test, and the power divider is used to divide the 10 MHz signal into two channels, one as the signal and the other as a reference. When the input reference signal is a square wave, the measurement results are shown in Fig. 2.

The measured second is 10^{-13}, which is equivalent to the floor noise of DDS. The noise of the tester itself may be better than the floor noise of the DDS. In order to further verify the testing capability of the tester for sine wave, the square wave was changed into sine wave for measurement, and the Allan variance curve obtained was shown in Fig. 3.

Using the signal source to generate any signal for measurement, the measurement is divided into two parts.

The first part is homologous measurement. The 10 MHz internal frequency standard signal output from the signal source is used as the reference frequency of the measuring instrument. The signal source is used to generate 4 MHz, 10 MHz, 20 MHz, 50 MHz and 80 MHz for measurement.

The second part is the measurement of different sources, using a crystal oscillator as a reference to measure another crystal oscillator, and then using this crystal oscillator to measure a rubidium atomic clock. The measured results are shown in Table 1.

It can be seen from Table 1 that in a wide frequency range, frequency measurement methods based on phase tracking can complete the measurement better.

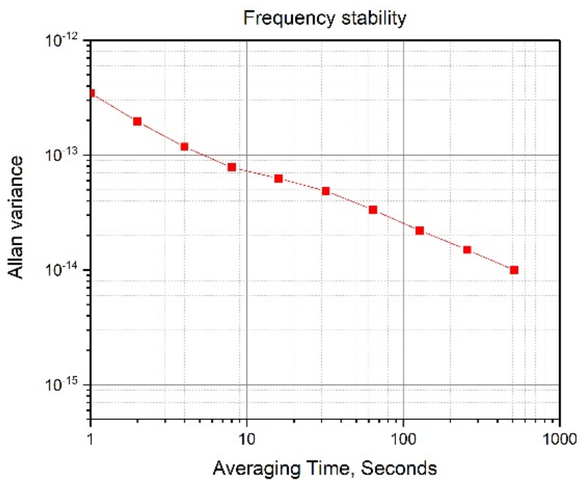

Fig. 2. Allen variance curve with floor noise of square wave measuring instrument.

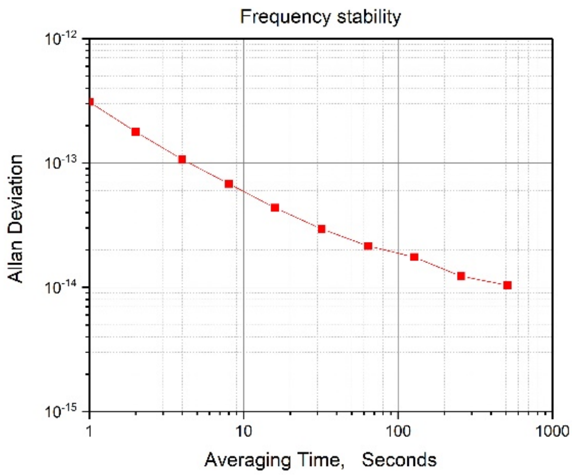

Fig. 3. Allen variance curve of the sinusoidal measuring instrument with floor noise.

Table 1. The phase tracking method was used to measure the signal stability at different frequencies.

f	τ		
	1 s	**8 s**	**128 s**
4 MHz	3.62×10^{-13}/s	7.12×10^{-14}/s	3.12×10^{-14}/s
10 MHz	3.11×10^{-13}/s	6.82×10^{-14}/s	1.75×10^{-14}/s
20 MHz	3.52×10^{-13}/s	6.65×10^{-14}/s	2.89×10^{-14}/s
50 MHz	3.41×10^{-13}/s	6.57×10^{-14}/s	3.02×10^{-14}/s
80 MHz	3.62×10^{-13}/s	6.45×10^{-14}/s	3.14×10^{-14}/s
Crystals-crystal	1.23×10^{-9}/s	7.42×10^{-10}/s	3.25×10^{-10}/s
Crystals- rubidium atomic clock	1.61×10^{-11}/s	7.53×10^{-12}/s	1.78×10^{-11}/s

The test result of frequency stability at 10 MHz is basically the same as that of direct self-test. It can be considered that the noise introduced by using signal source can be ignored.

In the crystals and crystal oscillator frequency ratio, the use of a crystal vibration for high stability crystal, its stability can reach 7.53×10^{-12}/s, as reference to measure another crystals and the crystals for the inside of a signal generator of crystals, tested its stability to 1.23×10^{-9}/s only, due to the stability of the high stability crystal vibration is much higher than this, so you can think internal clock signal source and poor stability. When the rubidium atomic clock is used as the frequency standard to measure the crystal oscillator with high stability, the stability of the crystal oscillator is measured as 1.61×10^{-11}/s. However, due to the poor long-term stability of the crystal oscillator, a significant increase can be observed when the sampling time is 128 s, which is caused by the crystal oscillator drift [7].

6. Conclusions

To sum up, in this paper, DDS produced by ADI and STM32 produced by STMicroelectronics are used as the control carrier, and the frequency stability can be achieved 10^{-13} by continuously measuring the frequency of the measured signals without dead zone. During the experiment, it is found that MC10116 is used as the waveform conversion circuit. When sinusoidal wave is converted into square wave, a lot of noise will be introduced, which will seriously affect the measurement results. After theoretical analysis and experiment, the scheme of using operational amplifier as waveform conversion circuit is redesigned.

This paper expounds the DDS without dead zone and high precision frequency measurement equipment, achieve no dead band frequency measurement, can be applied to a variety of applications, meet the demand of different measurement, however still exist some deficiencies on the accuracy of measurement, plans to use the higher conversion digit ADC, late can avoid using operational amplifier circuit, At the same time, it can improve the measurement accuracy and reduce the measurement steps, and avoid the error caused by the resistance drift of the amplifier circuit.

Acknowledgements

The paper is supported by the National Natural Science Foundation of China (Grant Nos. 1177 3022 and 1187 3039).

References

[1]. D. B. Sulliivan, D. W. Allan, D. A. Howe, F. L. Walls, Characterization of Clocks and Oscillators, *NIST Techniacl Note 1337*, 1990.

[2]. Allan D. W., Statistics of atomic frequency standards, in *Proceedings of the IEEE*, Vol. 54, Issue 2, 1996, pp. 221-230.

[3]. Zhou Xuyang, Research on Ultra-high Resolution Frequency Measurement Based on Phase Processing, 2015.

[4]. Yuan Shiliang, Dong Jie, Xu Zhiqiang, *et al.*, DFT correction algorithm for Phasor and Electrical volume based on Frequency Measurement, *Power System Protection and Control*, Vol. 46, Issue 14, 2018, pp. 128-133.

[5]. Zhou Wei, Wang Hai, Development of Time-frequency Measurement and Control Technology, *Journal of Time and Frequency*, Vol. 026, Issue 002, 2003, pp. 87-95.

[6]. Ma Ai-Wen, Qu Xing-Hua, The Quantized Redefinition of the SI and its Signification, *Acta Metrologica Sinica*, Vol. 41, Issue 2, 2020, pp. 129-133.

[7]. Zhu Xisong, State Space System Identification Algorithm and its Application in Frequency Measurement, 2020.

Sensors & Transducers, Vol. 254, Issue 7, December 2021, pp. 16-21

Sensors & Transducers

Published by IFSA Publishing, S. L., 2021

http://www.sensorsportal.com

Research on the Relationship between Phase Synchronization and Frequency Stability in Atomic Clock Circuit

[1] Nana Feng, [2] Miao Miao, [2] Zhiqi Li, [2, *] Wei Zhou and [3] Zhuang Cai

[1] Yan'an University, Area A, Chuangxin Port Campus, Xi'an Jiaotong University,
Chang'an District, Xi'an City, Shaanxi Province, 716000, China

[2] Xidian University, No. 2, Taibai South Road, Xidian University,
Yanta District, Xi'an City, Shaanxi Province, 710071, China

[3] Shaanxi Hua Xing Electronic Information Group co., LTD,
No. 16 Wenhui East road, Xianyang City, 712000, China

[1] Tel.: 13572973973

E-mail: wzhou@xidian.edu.cn

Received: 25 October 2021 /Accepted: 7 December 2021 /Published: 30 December 2021

Abstract: The implementation of the atomic clock circuit usually adopts frequency processing scheme. However, the quantization error in frequency processing greatly limits the frequency stability of the atomic clock's output from theoretical calculations. This paper analyzes the cause of quantization error and its relationship with the degree of signal synchronization. Based on this relationship, we study the effect of phase synchronization on frequency stability and explore how to effectively suppress quantization errors to improve measurement accuracy. Experiments show that using the regularity of phase information obtain continuous and lossless phase information. It can improve the accuracy of the gate acquisition and reduce the influence of quantization errors. Frequency stability can be improved from $1/\tau^{1/2}$ to $1/\tau$. The research on this relationship can be applied in various fields, such as high precision measurement of time and frequency, communication technology, navigation signal processing, and even defense science and technology for essential improvements.

Keywords: Frequency stability, Phase synchronization, Frequency measurement, Frequency processing, Quantization error.

1. Introduction

It is the highest accuracy and stability of frequency and time [1-2]. Measuring frequency and time is the most important activities for many fields [3-4], such as radar navigation, mobile communications, aerospace and navigation, geological exploration and other fields. The frequency source measurement accuracy cannot meet the theoretical requirements. Thus, improving measurement precision is a common issue. The frequency stability of the hydrogen atomic clock changes with time along $1/\tau$ (developed by the Shanghai Astronomical Observatory in 2006 [5]). The frequency stability of the crystal oscillator below a few seconds also conforms to the law of change. This phenomenon is the same as the trend of the phase processing law derived from the control of the phase-continuous atomic energy level transition phenomenon [6]. Passive atomic clocks, such as rubidium clocks and cesium clocks use frequency processing schemes, and its medium and long-term stability changes $1/\tau^{1/2}$ as time goes on. Products implemented by phase processing show higher frequency stability. However, owing to insufficient understanding of the complex phase phenomenon and the complicated of structure for phase processing. The frequency-based processing scheme appears in many precision frequency source [7]. In order to achieve high accuracy, it is further researched that frequency stability changes from $1/\tau^{1/2}$ to $1/\tau$. This paper uses phase synchronization processing to obtain continuous phase information, studies the influence of phase synchronization degree on phase information, and effectively controls the switching position of the gate to suppress the quantization error caused by ADC, thereby improving the frequency stability of the standard devices.

2. The Relationship between Quantization Error and Phase Synchronization

In high-precision frequency measurement, the measurement accuracy of instruments and meters is subject to certain limitations due to interference from process defects, complex circuits, and noise. Especially, when the analog signal is converted into digital signal, part of the phase information of the output signal is lost due to phase asynchrony, resulting in a deviation between the output value and the actual input value. The actual input and output signal difference size is related to the number of ADC quantization bits, that is, the sampling rate decreases as the number of ADC bits increases. Due to the limited number of ADC bits, the resolution of the measurement is limited, resulting in inherent information loss in the quantization process of analog signals. High-precision measurement can be obtained with high-digital ADC for digital measurement, but it is still inevitably affected by quantization error, conversion rate, signal bandwidthand so on. These factors limits its application [8]. Digitization makes the phase continuity can be better obtained during atomic energy level transitions. Different state of phase synchronization causes different phase information loss in the output signal, which can result in quantization error between the output value and the actual input value [9]. The quantization error is related to ADC (Analog-to-digital converter) bits.

When input voltage U is constant, several or several adjacent sampling points of the output signal are quantized to the same digital value due to noise interference. The sampling points change step by step within a period, this is the fuzzy area ΔR [10], which can be calculated by

$$\Delta R = LSB = \frac{1}{2^N}U \ , \tag{1}$$

where LSB is the least significant number, N is ADC bits and U is input voltage. Eq. (1) sees that fuzzy area is equal to least significant bit. Or fuzzy area ΔR can also be obtained by knowing the voltage and the number of ADC bits. The center position of fuzzy area is closer to true value, but it is technically difficult to achieve [11].

Therefore, the actual difference value of input and output or ADC quantized voltage value needs to be continuously corrected according to the distance from the border to the center. And it can only be infinitely close to the true value. However, the maximum quantization error is expressed by

$$\Delta V = \frac{1}{2}\Delta R = \frac{1}{2}LSB \ , \tag{2}$$

where ΔV is the maximum quantization error. For N-bit ADC, the half of the fuzzy area is called maximum quantization error. Meanwhile, the maximum quantization error can be expressed as 1/2 LSB.

For a measurement system, the magnitude of the ADC quantization error directly affects the accuracy of the sampling position. For a multi-period sampled input signal, the adjacent sampling points change in a single direction at fixed time intervals, that is, increase or decrease. When data points are strictly synchronized between transition border and sampling clock. The sampling points can sequentially cover all phase information. There is a flat area after sampling, in which the ideal phase coincidence point is hidden and difficult to capture. Therefore, the border of fuzzy area is selected as the flag of gate switch to improve the resolution of measuring equipment and finally achieve better accuracy. The accuracy improvement factor is expressed by quantized fuzzy area and the stability of quantized fuzzy area. Therefore, the accuracy improvement factor is calculated by

$$A = \frac{\Delta R}{\Delta\delta}, \tag{3}$$

where A is the accuracy improvement factor, ΔR is the quantized fuzzy area, $\Delta\delta$ is the stability of quantized fuzzy area, which is determined by the slight deviation of δ_1 and δ_2. The calculation formula of $\Delta\delta$ is

$$\Delta\delta = \delta_1 - \delta_2 \, , \tag{4}$$

where $\Delta\delta$ is much smaller than δ_1 and δ_2. The slight deviation of δ_1 and δ_2 is respectively error value at the switch gate and is also the interval between ideal gate and actual gate. The size of quantized fuzzy area $\Delta\delta$ is related to the resolution. Principle of quantization error suppression is shown in Fig. 1.

Where the bottom line is actual gate. The middle line is ideal gate. The top line is the selected border.

It can be seen from Fig. 1 that actual position is different from ideal position. The ideal door signal is difficult to capture. The quantization border has the highest stability and the highest accuracy. Therefore, selecting the value at the border is regarded as the switch flag of the measurement gate.

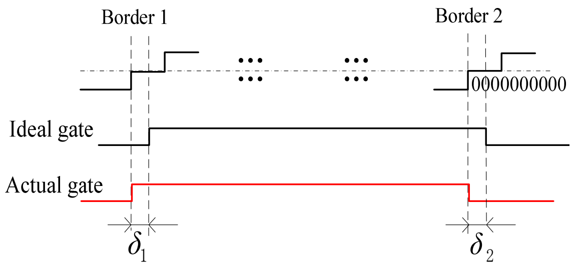

Fig. 1. Principle of quantization error suppression.

It can be discarded the background of circuit of random noises, such as noise and environmental noise. Although the selected location is different, the relationship between actual sampling point and ideal point is the similar. The total gate time remains unchanged so that it is closer to the true phase coincidence point or the true value. The method of selecting the gate by the border effectively offsets the measurement fuzzy area caused by ADC quantization. Therefore, the value at the border of the sampling point can effectively suppress the problem of insufficient ADC quantization resolution. Quantization error can be eliminated and phase synchronization greatly is improved, thereby improving the accuracy of its measurement control.

The actual error is different from the ideal error. However, the actual error can be expressed as

$$\Delta V^{'} = \frac{1}{2}\Delta\delta = \frac{\Delta R}{2A} = \frac{1}{2A}LSB, \tag{5}$$

where $\Delta V'$ is the actual error, which is half of the stability of quantized fuzzy area. And the ratio of ΔR to 2A is expressed as $\Delta V'$. Of course, the actual error can be calculated by the ratio of LSB to $2A$.

3. Experiments and Analysis of Different Phase Synchronization Degrees

3.1. Experimental Scheme

The precision frequency measurement of block diagram is shown in Fig. 2. The two-way signals meet the same frequency and have a small frequency difference. One way is measured signal $f_1=\Delta f+f_0$ and clock signal f_r, the other way contains reference signal f_0 and clock signal f_r. Clock signal f_r is the special and stable intermediary source signal. f_r only serves as an intermediate bridge, avoiding two signals between f_0 and f_1 direct comparison.

It can be seen from Fig. 2, two-way signal is sampled by dual-channel ADC to get Δf_1 and Δf_2. The sampling data of ADC is received in FPGA. Due to noise interference, filter is required to filter out the influence of random noise. The gate opening and closing time can be generated. N_0 and N_1 are calculated by the gate time signal generation circuit in FPGA. Two-way count value can be sent to MCU by serial communication protocol. The error signal ε is calculated by MCU. ε is generated by frequency difference that has been set $\Delta f'$ and the actually obtained frequency difference Δf. Then, ε is converted into a corresponding voltage u_c by DAC. VCXO is driven by u_c for precise frequency control in a closed loop. The correction of the measured signal frequency has been achieved by real-time adjustment signal frequency.

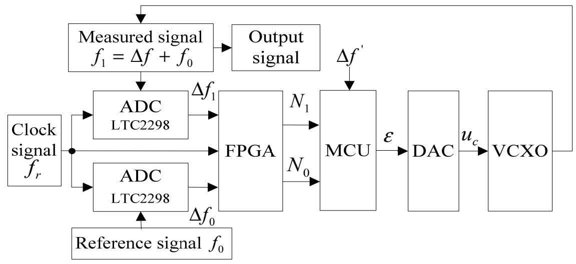

Fig. 2. Block diagram precision frequency measurement.

Within the period required for the phase of the measured signal and the reference signal to completely coincide, relative phase deviation between reference signal and measured signal is arithmetic series is calculated by

$$\Delta T = \frac{f_{\max c}}{f_0 f_1}, \tag{6}$$

where ΔT can reach the order of picoseconds. ΔT is step value in arithmetic series, that is, quantized phase shift resolution. $f_{\max c}$ is the frequency of greatest common factor. The reciprocal of $f_{\max c}$ is the least common multiple period, that is, the period required for the phase of the measured signal and the reference signal to completely coincide with each other, f_0 is reference signal and f_1 is measured signal. For the same frequency signals with a small frequency difference, if frequency difference is smaller, the sampling point ΔT is smaller. Therefore, in a least common multiple period, measured signal moves more subtle in phase, and phase information is more complete. For inter-frequency signal, the change of phase difference is often not monotonous but a chaotic change. If the step value of the phase difference between the signals is sorted out of order, it will be found that the step value is still ΔT.

The equivalent counting period and the frequency difference are calculated by

$$T_i = N_j * \frac{1}{f_r}(i, j = 0,1), \tag{7}$$

$$\Delta f_i = \frac{1}{T_i} = \frac{f_r}{N_j}(i, j = 0,1), \tag{8}$$

where T_i (i=0,1) is the equivalent counting period, N_j (j=0,1) is count value of two-way. Equivalent counting period of two-way can be calculated by count value N_j (j=0,1) and clock signal f_r. Δf_i (i=0,1) is the frequency difference, which has a common intermediate signal. The reciprocal of the equivalent counting period is Δf_i. Of course, Ratio of clock signal and count value of two-way is also expressed as Δf_i. In order to eliminate the influence of common intermediate signals on its results, according to Eq. (6) - Eq. (8), the relationship between f_1 and f_0 can be obtained by

$$f_1 = \left[\frac{N_1 - 1}{N_1} \times \frac{N_0}{N_0 - 1}\right] \times f_0 \tag{9}$$

According to Eq. (9), f_1 can be calculated by N_0, N_1 and f_0. Frequency difference between measured signal and reference signal in the text specifically refers to the frequency deviation between the input signal and the output signal. Frequency difference is calculated by

$$\Delta f = f_1 - f_0 = \frac{N_1 - N_0}{N_1(N_0 - 1)} \times f_0, \tag{10}$$

where Δf is frequency difference. The input reference signal f_0 is known. Therefore, the frequency difference can be calculated using the input signal and N_0 and N_x. The output frequency achieves automatically adjusted by Δf.

3.2. Frequency Stability Measurement under Different Frequency Correction

In order to verify measurement accuracy for experimental platform, input terminal f_r and tested terminal f_1 are connected to input and output of the measuring system. Both f_r and f_1 use 8607 as the reference source. The high-stability AFG3101C signal generator is used as a clock signal. (10M-1) Hz is selected by 8607 as an external frequency standard. The frequency stability can be calculated as shown in Fig. 3.

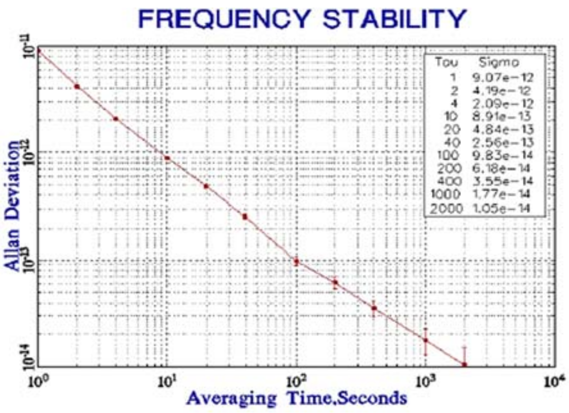

Fig. 3. Characteristic of frequency stability in verifying measurement accuracy experiment.

It can be seen from Fig. 3 that the second-level stability has reached 9.07×10^{-12}. And the thousand-second-level stability has reached 1.77×10^{-14}. At this time, the frequency stability varies along $1/\tau$ as time goes on.

In order to further study the relationship between phase synchronization and frequency stability, different frequency correction values can be selected. 10 MHz of ultra-high stability OCXO 8607 is regards as reference source of Tektronix AFG3101C signal generator, which accesses to the reference signal f_0. The clock signal f_r is set to (10M-1) Hz. Measured signal f_1 is set to 10 MHz from VCXO. The output frequency $f_1 = f_0 + \Delta f$ can be set to different frequency correction values by connecting with output of VCXO, such as (10M+1) Hz, (10M+2) Hz, (10M+4) Hz, (10M+8) Hz, (10M+10) Hz, (10M+20) Hz. Thus, measurement results of different frequency correction values are shown in Table 1.

Table 1. Measurement results of different frequency correction values.

Δf / Hz	**Δ*T***	**Second-level stability**	**Long-term stability**
20	2.00×10^{-13}	1.99×10^{-7}	1.00×10^{-8}
10	1.00×10^{-13}	$6.32\times10^{--10}$	1.25×10^{-11}
8	8.00×10^{-14}	7.92×10^{-10}	1.10×10^{-11}
4	4.00×10^{-14}	2.89×10^{-10}	6.25×10^{-12}
2	2.00×10^{-14}	1.55×10^{-10}	4.10×10^{-13}
1	1.00×10^{-14}	7.07×10^{-12}	2.55×10^{-14}

As shown in Table 1, Δf is different frequency correction values. ΔT is quantized phase shift resolution, shown in Eq. (6).

When Δf =1 Hz, the second-level stability of the output signal is the same as that of the verification measurement accuracy experiment, reaching the order of 10^{-12}. Compared with the verification accuracy experiment, the second-level stability has reached the order of 10^{-12}. When the frequency stability of 1000 s and 2000 s, it can reach the order of 10^{-14}. Therefore, the measurement accuracy is basically the same. In fact, when the phase synchronization accuracy reaches a certain level in the process of system measurement and control, the gate opening and closing flag is more accurate. The system will maximize the suppression of errors, making the output result closer to the true value of the fuzzy area.

When the frequency difference is (1~2) Hz, the theoretical quantization resolution ΔT can reach $(1\sim2)\times10^{-14}$ seconds; when the frequency difference is (4~20) Hz, the measurement resolution ΔT can reach $(2\sim10)\times10^{-13}$ seconds. The phase synchronization accuracy of the signal changes from 10^{-14} to 10^{-13}, and the long-term frequency stability of the frequency source changes from 10^{-14} to 10^{-8} as time goes on. If the phase is continuous when different frequency correction values is 1 Hz. Then, the quantization resolution is too large when different frequency correction values is 20 Hz. The phase is not continuously sampled. There is a certain gap, and a problem of phase loss.

Experimental result shows that there will have different quantization phase shift resolution and different phase synchronization accuracy under the same hardware conditions. At the same time, the frequency stability will show different changes with the sampling time. For example, the law of frequency stability with time shows $1/\tau^{1/2}$, $1/\tau$ or between $1/\tau^{1/2}$ and $1/\tau$. The frequency deviation of the measured signal can directly affect the resolution of phase processing and the accuracy of phase synchronization. Phase synchronization further affects the determination of the opening and closing time of the virtual gate. Waveforms of frequency stability changes of different correction values are shown in Fig. 4.

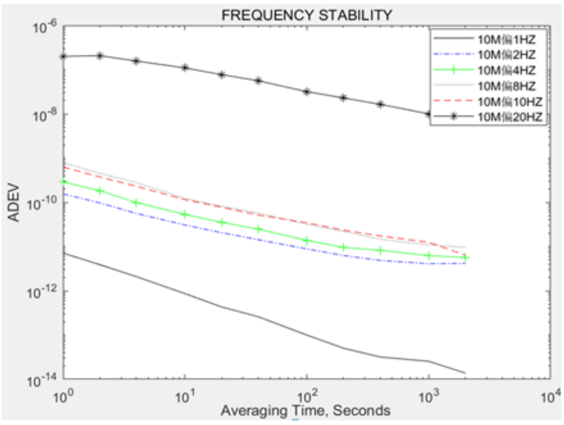

Fig. 4. Waveforms of frequency stability changes of different correction values.

It can be seen from Fig. 4 that as the frequency difference Δf increases, the frequency correction value is different and the quantization phase shift resolution ΔT will also change. The continuity of the phase information of the measured signal and its precision affect the control time of the phase noise on the frequency stability, which in turn affects the accuracy of the gate opening and closing. Fig. 4 shows that the frequency correction value is continuously increased by multiples and the frequency stability is continuously reduced with the continuous increase of the quantization phase shift resolution. That is, the accuracy of phase synchronization between signals is increased, and the information between phases is more comprehensive. Finally, quantization errors can be suppressed, which is expressed as frequency stability of changes from $1/\tau^{1/2}$ to $1/\tau$ as time goes on.

4. Conclusion

In this paper, the cause of the quantization error has been analyzed in digital frequency processing. It has researched the influence of phase synchronization degree on phase information. So the border of the fuzzy area have been selects as the gate switching signal to enhance the problem of phase information loss in traditional frequency processing. The research shows that the phase synchronization accuracy directly affects the continuity of the phase information and thus controls the frequency stability of the frequency source.

Acknowledgements

The paper is supported by the National Natural Science Foundation of China (Grant Nos. 11773022 and 11873039), and Research Project of Shaanxi Provincial Department of Education (20JK0983).

References

[1]. S. Sturm, F. Köhler, J. Zatorski, *et al*., High-precision measurement of the atomic mass of the electron, *Nature,* Vol. 506, Issue 7489, 2014, pp. 467-470.

[2]. W. Zhou, W. Hai, The development of time-frequency measurement and control technology, *Journal of Time and Frequency*, Vol. 26, Issue 2, 2003, pp. 87-95.

[3]. F. Milano, A. O. Maniavacas, Frequency-dependent model for Transient stability analysis, *IEEE Transactions on Power Systems*, Vol. 34, Issue 1, 2019, pp. 806-809.

[4]. O. Montenbruck, P. Steigenberger, L. Prange, *et al.*, The Multi-GNSS Experiment (MGEX) of the International GNSS Service (IGS) – Achievements, prospects and challenges, *Advances in Space Research*, Vol. 59, Issue7, 2017, pp. 1671-1697.

[5]. Z. Cao, The application and development of high-stability atomic clocks in space, *Aerospace Measurement Technology*, Issue 1, 1987, pp. 58-64.

[6]. C. Peter, B. Dan, G. Ramesh, *et al*., Low Noise Chip Scale Atomic Clocks (LNCSAC), in *Proceedings of the IEEE International Frequency Control Symposium (FCS)*, 2014, pp. 1-4.

[7]. N. Shiga, M. Takeuchi, Locking the local oscillator phase to the atomicphase via weak measurement, *New Journal of Physics*, Vol. 15, Issue 2, 2014, pp. 23-34.

[8]. L. Angrisani, M. D. Apuzzo, D. Grillo, *et al*., A new time-domain method for frequency measurement of sinusoidal signals in critical noise conditions, *Measurement*, Vol. 49, 2014, pp. 368-381.

[9]. L. Bai, X. Su, W. Zhou, *et al*., On precise phase difference measurement approach using border stability of detection resolution, *Review of Scientific Instruments*, Vol. 86, Issue 1, 2015, pp. 015106.

[10]. R. W. Fox, J. A. Sheman, L. S. Ma, *et al*., Making optical atomic clocks more stable with 10~16 level laser stabilization, *Nature Photonices*, Vol. 5, Issue 3, 2011, pp. 158-161.

[11]. H. Zhou, Z. Xuan, W. Zhou, Approach to the frequency standard comparison based on the equivalent phase comparison frequency, *Electronic Science and Technology*, Vol. 4, 2004, pp. 25-27.

Sensors & Transducers, Vol. 254, Issue 7, December 2021, pp. 22-30

Sensors & Transducers
Published by IFSA Publishing, S. L., 2021
http://www.sensorsportal.com

A Measurement Method Considering Both Phase Noise and Full Frequency Stability

[1] Wei Zhou, [1 *] Miao Miao, [1] Huifang Liu, [2] ChenceYang and [2] Bayi Qu
[1] School of Electro-Mechanical Engineering, Xi'dian University, Xi'an 710071, Shaanxi, China
[2] School of Information Engineering, Chang'an University, Xi'an 710064, Shaanxi, China
Tel.: 13892861331
E-mail: wzhou@xidian.edu.cn, mmiao@mail.xidian.edu.cn

Received: 25 October 2021 /Accepted: 29 November 2021 /Published: 30 December 2021

Abstract: The current mainstream phase noise measurement systems use the reference signal and the measured signal to achieve phase quadrature control after mutual locking, and then through phase information sampling, algorithm processing to get the single-sideband phase noise curve. A novel digital linear phase comparison method - DLPC can automatically keep the orthogonal phenomenon of the signal under test without lock processing. Therefore, it is easy to use and work more stable. This method is different from the traditional method, including the digital DMTD. That is, the frequency stability sampling time corresponding to the deviation of the carrier frequency from 1 Hz to 1 MHz or 10 MHz in the usual phase noise measurement is also the stability index from 1 second to 1 μs or 0.1 μs, respectively. The frequency stability measurement of DLPC can cover the period from the signal carrier frequency to the unlimited time. The new method works more stably, especially in the case of noise interference and poor stability of the measured signal, and lock loss will not occur. At the same time, the new technology can measure the phase noise in time domain and frequency domain simultaneously, and can fully reflect the noise essence of frequency source and the effect of noise influence.

Keywords: Digital, Linear phase comparison, Phase noise measurement, Phase quadrature control, Frequency stability, Carrier frequency.

1. Introduction

Single-sideband phase noise measurement technology plays an important role in the noise analysis of frequency sources and the improvement of its performance. Although the research on phase noise measurement has been conducted for many years, its equipment is complicated and inconvenient to use, especially difficult to obtain information on both time and frequency domain at the same time. Therefore, it is expected that phase noise of frequency domain and frequency stability of time domain can be displayed in one-to-one correspondingly, while its equipment is reasonable simplification and more convenience. In this way, its users could be more fully acquainted the noise of the measured frequency source and its impact.

The current mainstream single-sideband phase noise measurement systems use the reference signal and the measured signal to achieve phase quadrature control after mutual locking, as the Fig. 1 shows [1, 2].

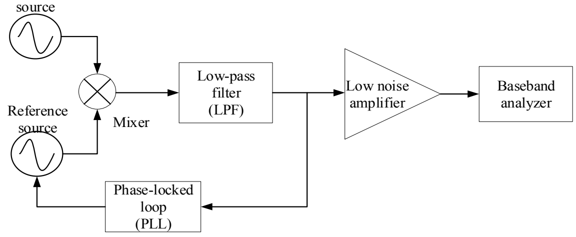

Fig. 1. Loose phase locking method in traditional phase noise measurement.

Its purpose is to realize that the two comparison signals can be completed in phase quadrature, use the reference signal and the measured signal to achieve phase quadrature control after mutual locking and then through phase information sampling, algorithm processing to get the single-sideband phase noise curve. However, the equipment is complicated and expensive, and the operation is also complicated. The response time sometimes is very long, and the stability of the quadrature lock is affected by big noise changes [1].

The digital linear phase comparison method to be involved in the paper firstly realizes the linear representation of the phase change, from 0 to 360 degrees, of the measured signal; achieves the phase noise measurement through researching the algorithm of single-side band phase noise measurement. Because of the ability to measure transient and short-term frequency stability quickly, we are also capable of accomplishing the corresponding measurement between frequency stability in time domain and phase noise in frequency domain.

2. Digital Linear Phase Comparison

The operating condition that the mainstream phase noise measurement system should guarantee, which is the phase quadrature between compared signals can actually be achieved without phase locking. The digital phase comparison DLCP [3-5] between multiple frequency relationships can reflect the natural characteristic that must exist when measured signals in phase quadrature state [5-6]. In digital measurement, when the clock signal frequency is n times (e.g. 10 times) of the measured signal, there will have n relatively stationary sampling clock signals in a period of the measured signal. As Fig. 2 shows, there will always be a clock signal sampling in the phase "quadrature zone" where is at the rising segment and close to the zero phase of the measured signal. In this way, the original full-period phase change of a measured signal converts into n phase difference changes which have 1/n original period and higher sensitivity with an excellent linearity. It is shown in Fig. 3. Whether frequency stability measurement in time domain or phase noise measurement in frequency domain, the phase change rate of the measured signal, $\Delta T/\tau$ ($\Delta f/f = \Delta T/\tau$), is detected and collected, where ΔT is change in phase difference and τ is the time corresponding to phase difference change. From the measurement of phase difference variation, this kind of conversion does not have an influence on phase continuity of signal, which is the variation characteristic of voltage-phase which originally performance in sinusoidal form be converted into an orthogonal representation of n segments.

The phase change from 0 to 360 degrees at lower phase comparison frequency (for example 10 MHZ) is decomposed into several phase changes from 0 to 360 degrees at higher and multiple phase comparison frequencies (for example 100 MHz) with higher resolution. The resolution of the measurement essentially depends on the stability of the AD conversion and its noise characteristics. AD conversion border effects will break through the 100 fs resolution limitation.

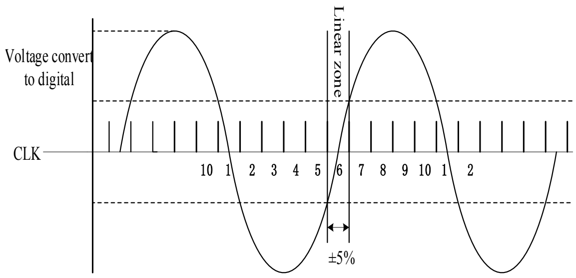

Fig. 2. The digital method of sine waveform linear segment high-frequency clock corresponding to sequence digital phase sampling.

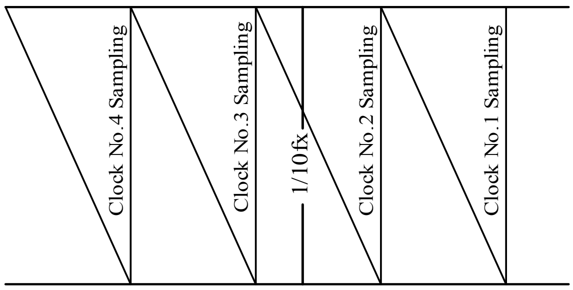

Fig. 3. Phase detection output signal of linear phase processing.

It is undeniable that the current technical indicators in the measurement are affected by the noise of the clock multiplication circuit. Improvement in this area is also one of the keys. Of course, this effect is similar to that of the frequency synthesizer used in the traditional method.

Regarding the problem of the noise effect of the clock signal, several solutions have been proposed. The variety of measured signal frequencies sometimes also provides the simple choice that not required the clock signal frequency doubling. In another aspect, the advantageous combination of multiple references also enables a higher measurement precision with increasing reference and the processing of measured data without doubling frequency, that is, we can avoid the problem of clock frequency doubling. The hardware is not implemented to realize phase-locked frequency doubling, instead, it goes through multiple high-resolution testing sessions, the noise that should be eliminated can be detected and use the software calculating to removing. The way dual AD shares the clock has been experimented with, and it has few effects [6].

The principle block diagram of the system is shown in Fig. 4.

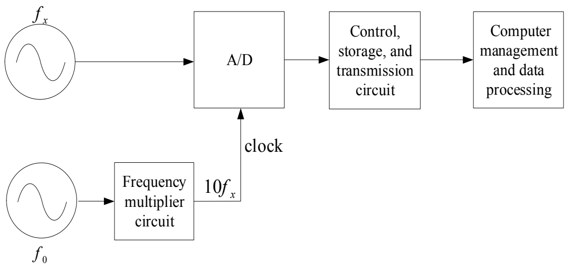

Fig. 4. Principle block diagram of the DLPC system.

The equipment based on the scheme has been conducted to perform a large number of full-frequency stability measurements with different frequency sources, which make sure the transient stability measurement with the carrier period as the shortest sampling time. Therefore, information omitted before can be obtained. The following figures are the results of self-calibration of ultra-high stability crystal oscillator OCXO 8607 (Fig. 5), crystal oscillator measurement (Fig. 6), Cesium clock 5585B measurement (Fig. 7) and DDS output signal's frequency stability (Fig. 8) in full response time.

In the phase comparison process, the relationship between frequency difference and phase difference variations:

$$\frac{\Delta f}{f} = \frac{\Delta T}{\tau} \tag{1}$$

The calculation formula of frequency stability is as follows:

$$\sigma_y(\tau) = \frac{1}{\tau}\sqrt{\sum_{i=1}^{m}\frac{(\Delta T_{i+1} - \Delta T_i)^2}{2m}} \tag{2}$$

For two compared signals, Δf is the frequency difference, f is the nominal frequency, ΔT is the phase difference change and τ is the comparing time.

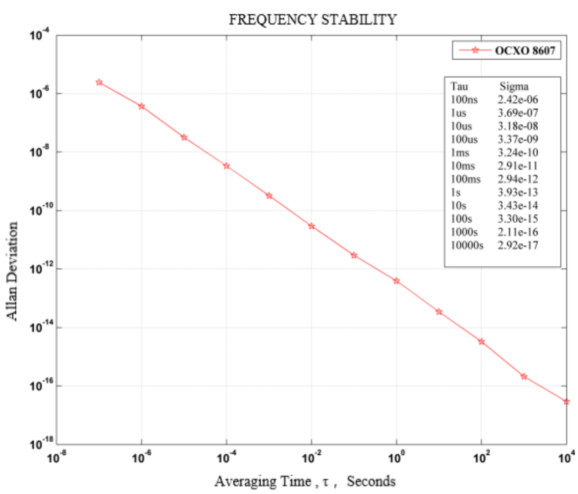

Fig. 5. Self-calibration frequency stability curve of OCXO 8607.

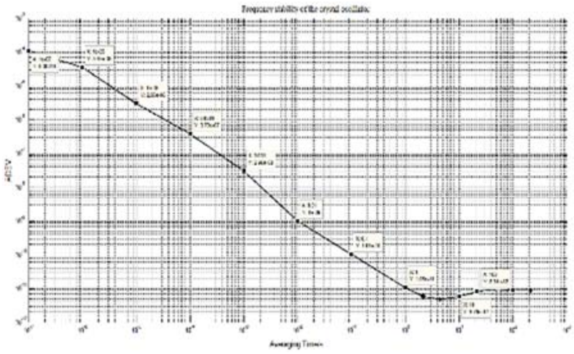

Fig. 6. Frequency stability of crystal oscillator in full response time.

The Cs atomic clock 5585B is compared with the ultra-high stability OCXO 8607, as shown in Fig. 7. The frequency stability of Cs clock 5585B are $<1.2\times10^{-11}$/s and $<8.5\times10^{-12}$/10 s, $<2.7\times10^{-12}$/100 s and $<8.5\times10^{-13}$/1000 s, which is measured by higher lever equipment. The frequency stability measured by the new type are 1.31×10^{-11}/s and 7.63×10^{-12}/10 s, 2.64×10^{-12}/100 s and 7.25×10^{-13}/1000 s, basically consistent with the above. From Fig. 7 it is shown that the frequency stability of Cs clock varies from $1/\tau$ to $1/\sqrt{\tau}$ with the average time changing.

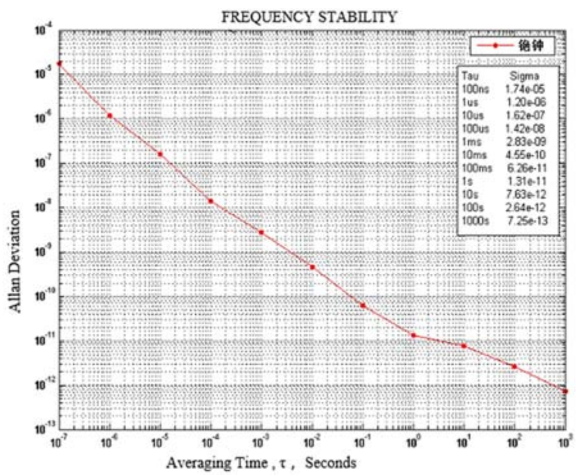

Fig. 7. Frequency stability curve of Cesium clock 5585B.

In Fig. 7, the horizontal axis shows the averaging time in s and the vertical axis the frequency stability, characterized by Allan Deviation.

It can be seen from Fig. 8, compared with high-stability crystal oscillators and atomic clocks, the transient stability of DDS is obviously poorer than the former two, due to the principle of DDS. The main parts of DDS are a phase accumulator and a look-up table. Because its output frequency is determined by searching step length, the spurs are relatively large, making its transient stability worse than crystal oscillators and atomic clocks.

Due to DDS control process of the crystal oscillator adopting phase processing, the frequency stability of DDS in Fig. 8 keeps in the slope of 1/τ with time.

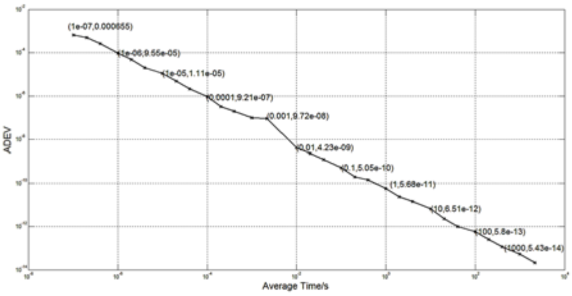

Fig. 8. Full response time frequency stability of DDS.

From the frequency stability of frequency source devices based on crystal oscillator, in full response time, it can be seen that the frequency stabilities of the main transient and short-term show the changing law of 1/τ with the sampling time. This embodies the characteristics of phase-modulated white noise. Comparing with each other, the short-term and the ultra-short-term frequency stability of different types frequency sources also could be known. From Fig. 5, Fig. 6 and other experiments, it can be clearly seen that a high-stability crystal oscillator, without being affected and controlled by other natural reference sources, often owns a changing law of 1/τ within a sampling time less than 1 s. While in longer than 1 s, the low-frequency noise and aging of crystal oscillators will worsen its frequency stability as the sampling time changes.

However, different situation will appear in passive atomic clocks, such as Cs clocks. About the transient frequency stability, we have raised it before a few years [6], but no attention should be paid. Nowadays, with the wide development of the periodic signal parameters measurement, in some measurements related to multiplication factors, especially in the time processing with a signal cycle as a phase step or in the measurement and processing on AC voltage signal, the most obvious effect is the signal's own transient frequency stability.

For the phase noise measurement of a single-frequency component signal, such as a common frequency standard signal, ADC's clock signal can be achieved just by frequency-multiplication. For the phase noise measurement of signals in a wide frequency range, it is necessary to cooperate with a low-noise frequency synthesis instrument used in traditional phase noise measurement systems. According to the measured signal frequency, it need to output a signal equivalent to 10 times frequency of the measured signal.

For the digital measurement of measured signal with higher frequency, it is difficult to always keep at 10 times frequency relation over the measured signal and the clock signal. In the aspect, there are also continuous iteration research, that makes the ADC's clock signal and the measured signal follow a relationship in the least common multiple period [2], to get the linear region of measured signal. In this way, the fastest response time will be shortened, while it also ensures that the clock signal is at a lower frequency and has a certain frequency difference relationship with the measured signal.

3. Time-domain Frequency Stability and Frequency Domain Phase Noise Measurement Based on Phase Information

The new measurement system use ADC as a linear phase discriminator, the phase comparison time can be set flexible with the help of FPGA, extracting the sampling point data in the linear section of the measured signal, the measurement of phase noise from the far carrier frequency to near carrier frequency can be realized. The system is using the spectral estimation algorithm, in order to improve the resolution and reduce the variance, after multiple groups of comparison experiments, the length and coincidence degree of the window are reasonably set. At the same time, to solve the problem of resolution fixed during FFT calculating, the segmentation and splicing of the frequency spectrum are designed, the high resolution and low consumption phase noise measurement is realized.

The 16 bit A/D converter is selected, when the reference voltage is 3.3 V, the quantization resolution can reach 50.35 μV. A 16-bit ADC with a relatively high sampling rate of 105 Msps, the LTC2217 of Yardenow is selected, the analog input range is 2.575VPP, the background noise is 81.3dBFS, the parasitic free dynamic range is 100 dB, and the ultra-low jitter is 85 f_{sRMS} [7].

The block diagram of the phase noise measurement system is shown in Fig. 9.

The working principle of the system is as follows: the frequencies of the system clock and the measured signal are in multiplication relationship, so the nominal frequency of the reference signal could be made the same as the measured, and then multiplied as ADC's clock to sample the measured signal. Using FPGA, the linear region of the sampled signal is judged and the phase difference information is extracted. When the data volume reaches the set value, the data is transmitted to the host computer, through the serial port, for power spectrum estimating and other related processing, and then the phase noise curve and frequency stability are obtained.

The system selects a 16-bit A/D converter. When the reference voltage is 3.3 V, the quantization resolution can reach 50.35 μV, which can meet the measurement requirements in most cases; the 16-bit ADC with a relatively high sampling rate, 105 Msps, is selected. ADC. LTC2217 is a 16-bit A/D converter with a sampling rate of 105 Msps, an analog input range of 2.75 Vpp, a noise floor of 81.3dBFS, a spurious-free dynamic range of 100 dB and an ultra-low jitter of 85 fs_{RMS}. With excellent noise performance, it is suitable for demanding communication applications.

The FPGA selected in this system is the Spartan-6 series of Xilinx manufacturer. This series provides leading system integration functions, meeting the needs of most users at a lower cost. The series has 13 members, provides an expanding density from 3840 to 147443 logic units, makes its connection faster and more comprehensive, achieves the best balance of cost, power consumption and performance and has been widely used. At the same time, we weigh the relationship between data extraction in linear region, data storage and chip power consumption, the XC6SLX9-2FTG256C chip of the Spartan-6 series is selected. The chip has 256 ports, up to 200 user-available I/O pins, 9152 logic units, and a maximum of 576 kB of Block RAM, which fully meets the system design requirements.

The design flow chart of multiple resolution power spectrum estimation is shown in Fig. 10.

The measurement of phase noise is mainly divided into two modules: phase difference information acquisition and data processing. The data processing module includes the processing of amplitude-phase conversion on the extracted data in the effective linear region, phase difference calculation and removal of gross errors, etc., to obtain the phase fluctuation information, and then, by estimating the power spectrum of the phase fluctuation information, realize the phase noise measurement.

Since the focus of the phase noise measurement is the change trend of the power spectrum curve, for a group of measured data, based on the Welch method, a single data segment average can be used to reduce the variance; at the same time, the appropriate data segment length and data overlap can be selected to perform power spectrum estimation.

In the process of power spectrum estimation, Fourier transform is an indispensable part. Because the FFT operating resolution is fixed, that is, in the result of an FFT operation, the distinguishing capabilities on the power spectrum are the same in the low frequency band and the high frequency band, which will result in waste of resources or low measurement accuracy [8]. For example, suppose that when the spectrum distribution is between 0-10 Hz, a resolution of 1 Hz is required. While, for the spectrum distribution between 100 k-1 MHz, if the resolution is still adopted at 1 Hz, more points will be required and the calculation speed will be slower, resulting in resources waste. However, factually there is no need to using such a high resolution at this stage. In order to balance the pros and cons of the FFT points and the resolution, we have adopted a method of segmenting the measuring frequency range. For different frequency bands, select different sampling frequencies to achieve its power spectrum estimation.

In this system, the phase difference data sampled by the ADC is extracted through FPGA in the linear region with the phase comparison time as the interval, and stored in FPGA. When the data quantity reaching the default value, the data will be transmitted to computer through serial ports, saved and processed by MATLAB software, to obtain its power spectrum distribution curve.

If the number of data points involved in the FFT operation is 2048, the frequency spectrum segmentation is shown as Table 1.

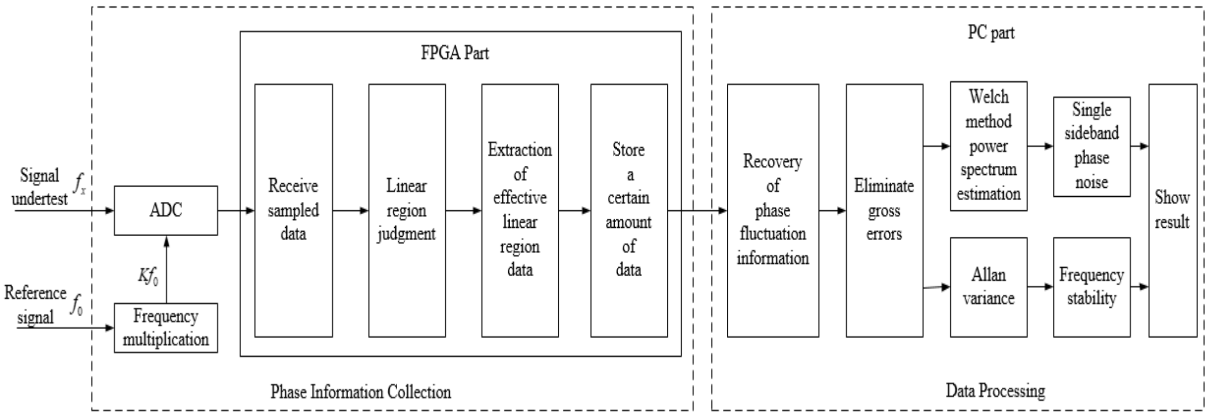

Fig. 9. System overall block diagram.

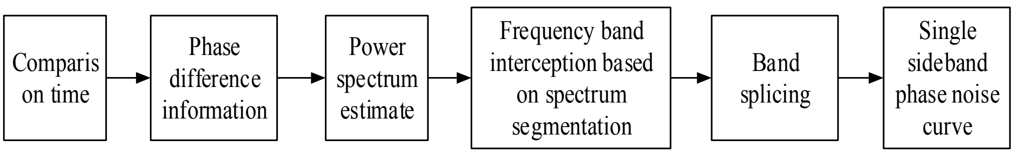

Fig. 10. Procedure diagram of the multi-resolution power spectrum.

Table 1. Spectrum segmentation situation.

Number of paragraph	Phase comparison time	Actual sample rate /Hz	Analysis bandwidth /Hz	Intercept frequency band /Hz	FFT points	Resolution /Hz
1	100 ns	10 M	0~5 M	100 k~1 M	2048	5k
2	1 μs	1 M	0~500 k	10 k~100 k	2048	500
3	10 μs	100 k	0~50 k	1 k~10 k	2048	50
4	100 μs	10 k	0~5 k	100~1 k	2048	5
5	1 ms	1 k	0~500	10~100	2048	0.5
6	10 ms	100	0~50	0~10	2048	0.05

By setting the phase comparing time, the segment processing of the spectrum can be realized. In the first segment, the bandwidth is 0~5 MHz and the frequency resolution is 5 kHz, which is the farthest band away from the carrier frequency, known as the far carrier frequency. Generally speaking, 5 kHz could almost meet the most frequency resolution requirements. In the sixth segment, the bandwidth is 0~50 Hz, and the frequency resolution is 0.05 Hz, which is the closest band the carrier frequency, also called as the near carrier frequency. This resolution can also meet the requirements of near carrier frequency. The division of frequency bands has satisfied the resolution requirements of the entire measurement range.

For the processing of spectrum splicing, when the number of FFT points is 2048, the number of points of the obtained single-sideband power spectrum result is 1024. Between [0, 10 Hz], a frequency band, it can be seen from $f_n=f_s{\cdot}n/N$ that [0, 1024], the number of points, represents [0, 50 Hz], the frequency range. Herein, the 205th point just is about 10 Hz, then [0, 205] represents [0, 10 Hz]. The point [206, 1024] represents the frequency range (10 Hz, 50 Hz], which belongs to the next frequency band and in which all points are discarded.

In [10 Hz, 100 Hz], the points number of [0, 1024] represents the frequency range [0, 500 Hz], in which [0, 20) represents approximately [0, 10 Hz). Because the above frequency band has been already analyzed on power spectrum, the points in the interval [0, 20) are discarded. The 205th point is about at 100 Hz, so the frequency range [10 Hz, 100 Hz]represents the point [20, 205]; the remaining points is corresponding to the next frequency band, so the points in the interval [206, 1024] are discarded.

In the same way, in [100 Hz, 1 kHz], the selected point interval is [20, 205]; in [1 kHz, 10 kHz], the point interval is [20, 205]; in [10 kHz, 100 kHz], the point interval is [20, 205]; in [100 kHz, 1 MHz], the point interval is [20, 205]. By splicing the spectrums obtained above, the power spectrum curve of the entire interval can be obtained.

If the spectrum segmentation is not used in the power spectrum estimation, let the phase comparison time to be 10 ms, to extract the data of the linear region of the measured signal with the analysis bandwidth of [0, 50 Hz]. The length of the window function is 512, and thus the frequency resolution is about 0.2 Hz. If such a high resolution is still adopted, for the high frequency band above 1 MHz, that at least $5{\times}10^7$ points are required, which will lead to too large calculation. However, according to the high frequency band, it is completely unnecessary to use such a high resolution. Therefore, spectrum segmentation method can solve the problem of fixed resolution for frequency spectrum estimation.

According to the multi-resolution power spectrum method proposed above, for the data of the phase difference in the linear region extracted by digital phase processing in this system, the single sideband phase noise curve is shown in Fig. 6, obtained by using Welch method and Hamming window to estimate the power spectrum. The figure reveals that different resolution could be able to obtained for different frequency bands. The method not only meets the resolution requirements, but also, to a certain extent, saves resources and improves the calculation rate.

When the Welch method [8] be adopted to do the multi-resolution power spectrum estimation, for the phase data that sampling point number nfft=2048, set the length of Hamming window as 512 and the degree of overlapping is 50 % to do the measurement about single sideband phase noise.

4. Phase Noise Measurement and Processing Algorithm and Experiment

In order to evaluate the functions and technical index of the novel phase noise measurement system, the comprehensive experiments and measurements are conducted, including the self-calibration experiment of the high-stability OCXO, the phase noise measurement of the rubidium atomic clock as the measured frequency source, and the full-frequency stability measurement. Through the above experiments, both the technical index and the correlation between the indexes of frequency stability and phase noise can be obtained at the same time, helpful to fully grasp the phase noise of the measured signal.

The final test results are shown in figures below. Among them, Fig. 11 is the result of mutual comparison of measuring the oscillator's own frequency by using the ultra-high stability crystal oscillator 8607 as a reference and frequency doubling to generate a clock signal.

The self-calibration experiment, shown in Fig. 12, is conducted using the 10 MHz output of OCXO 8607, one of that as the measured signal, and the other put into a signal generator, SMB100A, as the external reference to generate a frequency multiplied signal, which is the clock of ADC. FPGA is utilized to flexibly set the phase comparison time and sample the measured signal. The extracted phase difference data is transmitted to the host computer through the serial debugging assistant, and then made use of to estimate the power spectrum; at the same time, the phase difference data also is calculated to get the Allan variance, realizing the measurement of the full frequency stability.

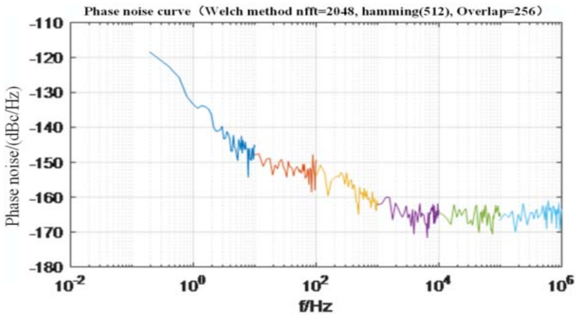

Fig. 11. Self-calibration stability and phase noise of 8607 crystal oscillator.

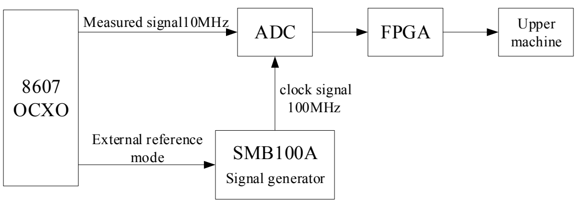

Fig. 12. Block diagram of self calibration experiment of the measurement system.

In the case of self-calibration of OCXO 8607 based on the new designed system, the frequency stability of 100 ns is 2.94×10^{-6}, the frequency stability of 1 s is 4.11×10^{-13}; while the frequency stability of 1 s by 3120A, the current internationally popular instrument, is 2.82×10^{-13}. Although there is still a certain gap between the method and 3120A in the short-term stability index, it cannot be ignored that the measurement range of the new method is much larger than 3120A, and has reached the whole range. Comparing to other measurement methods in the world, the method has significant advantages.

Fig. 13 shows the frequency stability (a) and phase noise (b) of a rubidium clock measured by this system.

The frequency stability measured here is the stability index, on the whole time range, of the rubidium atomic clock under test. The sampling time shown in Fig. 13(a) can range from the carrier frequency cycle of the signal under test, 100 ns, to more than 10 s, factually up to an unlimited time. Therefore, there is a one-to-one correspondence between the sampling time of frequency stability and the frequency deviation from the carrier frequency of the phase noise measurement, shown as Table 1. The correspondence has never been available before in any existing technologies. The frequency stability of a rubidium atomic clock changes with$1/\tau$ to $1/\tau^{1/2}$ variation to reflect the transformation from white noise of phase modulation to white noise of frequency modulation controlled by the atomic energy level transition [5].

This is not obvious from the phase noise diagram (b).

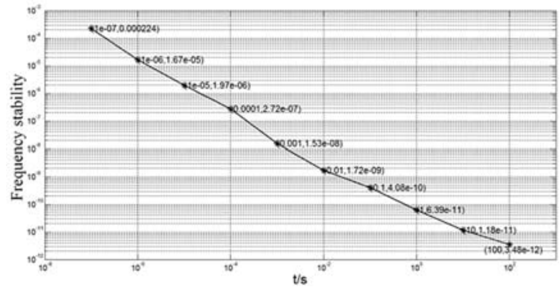

(a) frequency stability of Rb clock

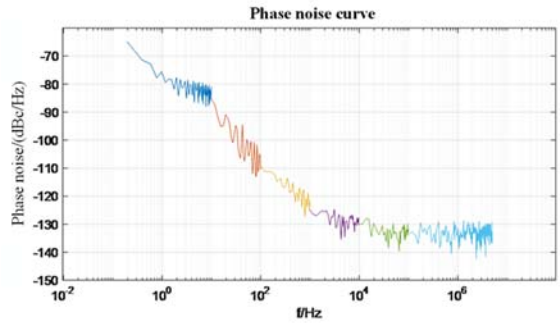

(b) phase noise of Rb clock

Fig. 13. The frequency stability (a), and phase noise (b) of a rubidium clock measured by this system.

Table 2 shows the comparison between the measurement results of rubidium atomic clock using the system introduced in this paper and PN8010 system produced in France.

Table 2. The comparison of rubidium atomic clock phase noise measurement results.

Frequency offset (Hz)	PN8010 (dBc/Hz)	Our system (dBc/Hz)
1	-70.2	-75.5
10	-82.6	-83.7
100	-111.3	-109.6
1 k	-126.8	-123.9
10 k	-134.5	-130.9
100 k	-136.4	-133.2
1 M	-138.3	-135.9

Errors in the phase noise measurement system designed in the paper mainly includes ADC sampling error, clock jitter error, sampling point selection error and frequency multiplication error.

1) ADC sampling error.

In the digital measurement system, due to the limitation of ADC's quantization bits, it is inevitable that there is quantization errors in the measurement process. Here, under the condition of ensuring the sampling rate, LTC2217, an analog-to-digital converter, with a quantization bit of 16 bits is selected to meet the measurement requirements, considering the influence of the main parameters, such as signal-to-noise ratio, differential nonlinearity, integral nonlinearity, etc. the quantization error is as small as possible. Regarding the suppression of digital quantization errors, some new processing methods have been constantly tested, and better results will be obtained.

2) Clock jitter error.

In the process of ADC sampling, the clock signal is a time basis of the measurement system. The sample process is seemed as the multiplication of the measured signal and the clock signal in the time domain or the convolution in the frequency domain. Therefore, the frequency spectrum of the measured signal will be mixed with the frequency components of the clock signal, which appears as the measured signal's spectrum deviation from the sampling clock. It will cause the spectrum of the signal under test to be no longer pure, increasing the spectral line width and affecting the signal-to-noise ratio of ADC sampling (*SNR*).

3) Sampling point selection error in linear region.

In this measurement system, the measured signal is a sine signal. The slope of tangent line at each phase point of the sine signal is different, so that every quantization fuzzy area produced in the quantization process is also inconsistent. In the vicinity near zero phase point, that is, the linearization area of the phase change, the slope at the tangent point and the step value generated in the unit time are maximum, while the sensitivity relatively larger and the measurement error smaller. For two signals with K times multiplication, when sampling the measured signal by the digital linear phase comparison method, it will be sampled as K equispaced points in one cycle, taken $1/K$ out of the full-period near the positive zero-crossing point as the linear region. Obviously, one of the sampling points must fall within the linear region of the signal under test. As shown in Fig. 9, theoretically the larger K, the narrower the linear region and the closer to the positive zero-crossing point the position, the better the linearity, the greater the tangent slope, and the more accurate the measurement. However, the maximum sampling rate of LTC2217 limits K. In this measurement system, for the measured signal of 10 MHz, the maximum is up to K=10, so the linear region is 36°. If the sampling rate is higher, raising Kcan further reduce errors caused by the sampling points selection.

4) Frequency multiplication error.

In this measurement system, the clock signal of ADC is a 100 MHz sinusoidal signal that is multiplied from the reference signal by SMB100A. The noise of RF signal generator will inevitably be introduced into the measurement system during the conversion, which reduce the measurement accuracy. If OCXO 8607 is self-calibrated by directly phase-shifting without a frequency multiplier, the frequency stability of the self-calibration will reach 1×10^{-13}/s. Therefore, further improvements can be developed from this aspect.

5. Conclusion

In the research about single sideband phase noise measurement, there are some digital methods successfully [9-11]. Here our method is simpler and easy to combine with traditional technology. We use the digital linear phase comparison method to solve the problem that phase quadrature and abstract the phase change information can only be achieved by means of phase mutual locking in the traditional system. The function of this link simplifies the system, avoids the trouble caused by losing lock, improves the working efficiency, explains the differences in indicators between different frequency sources.

The linear segment (digital mode) which naturally exists in signal (sinusoidal) waveform can be effectively utilized to obtain satisfactory linearity. Due to limited of the phase variation region of the excellent linear segment under the condition of frequency relation multiplying, starting from the average frequency deviation $\Delta f/f = \Delta T/\tau$ relationship and frequency stability, this will not affect the measurement of the phase difference variation, frequency, and frequency stability. With the deepening of research, other technologies suitable for extracting phase orthogonal information in a wider frequency range will be developed, which is suitable for the wide application of commercial phase noise measurement system.

Acknowledgements

Supported by National Natural Science Foundation of China under No. 11773022 and 1187 3039.

References

[1]. D. L. Yan, Development of phase noise measurement technology, *Aerospace Measurement Technology*, Vol. 26, Issue 5, 2006, pp. 59-61.

[2]. W. Zhou, X. Ou, H. Zhou, The time frequency measurement and control technology, *Xidian University Press*, 2006.

[3]. A digital phase shift aided linear phase comparison method, *Patent 201910243834.*

[4]. A linear phase comparison method based on direct digital phase processing, *Patent 201910243847.5*.

[5]. W. Zhou, Z. Li, W. Qiao, The most potential technology in time frequency domain-Digital linear phase comparison, in *Proceedings of the China Conference on Time and Frequency (CTFS'2019)*, 2019.

[6]. Z. Wei, Z. Li, L. Bai, *et al*., Generalized phase measurement and processing with application in time-frequency measurement control and link, in *Proceedings of the 2013 Joint European Frequency and Time Forum and IEEE International Frequency Control Symposium*, 2013, pp. 429 - 433.

[7]. http://www.bdtic.com/en/linear/LTC2217.

[8]. Q. Ren, Y. Yu, Application of Welch power spectrum estimation algorithm in phase noise measurement, *Automation Instrument*, Vol. 35, Issue 1, 2014, pp. 19-21.

[9]. Allan Ecker, A Digital Method for Phase Noise Measurement, in *Proceedings of the IEEE International Test Conference (TC)*, Washington, 2012, pp. 1-10.

[10]. H. Gheidi, A. Banai, A New Phase Shifter-less Delay Line Method for Phase Noise Measurement of Microwave Oscillators, in *Proceedings of the IEEE European Microwave Conference*, 2008, pp. 325 - 328.

[11]. T. Imaike, Full digital phase noise measurement by using two reference oscillators and multichannel ADCs, in *Proceedings of the Joint Conference of the European Frequency and Time Forum and IEEE International Frequency Control Symposium ((EFTF/IFCS)*, 2017, pp. 583 - 586.

Sensors & Transducers, Vol. 254, Issue 7, December 2021, pp. 31-37

Sensors & Transducers
Published by IFSA Publishing, S. L., 2021
http://www.sensorsportal.com

Investigation of the Eigen Frequency of a Cantilever Microbeam Immersed in a Fluid Under the Piezoelectric Effect

[1, *] Victory ELIAS, [2] Flavie BRAUD, [3] Philippe CHAMPAGNE and [1] Georges NASSAR
[1] UPHF - INSA Hauts-de-France, IEMN - UMR CNRS 8520
[2] University of Lille-PhLAM-UMR CNRS 8523
[3] UPFF - INSA Hauts-de France, LMCPA
[1] Tel.: +33601842765, fax: +330327511722
E-mail: Victory.Elias@uphf.fr

Received: 19 October 2021 /Accepted: 30 November 2021 /Published: 30 December 2021

Abstract: In this paper, a new model of piezoelectric cantilever is developed, it can be heavily used in a micro electromechanical system (MEMS). This new prototype eliminates several risks caused by the previous means already used and increases the sensation in terms of rheology. Our approach is based on the approximation of the Eigen frequency shift when the micro-beam is totally immerged in an incompressible fluid. The density variation of the fluid is deduced and solved according to the behavior of the Eigen frequency. The material used for the manufacturing of the cantilever beam is Silicon Dioxide or Silica which is a porous material. Moreover, if the fluid contains particles, they can be adsorbed on the pores of the micro-beam and cause a change in the mass. Examination of theoretical computation by simulation approach was done using COMSOL Multiphysics software. The self-sensing micro-cantilever obtained in vacuum is around 390 Hz/ng measured at a center frequency of 960 kHz and with a density resolution of 0.055 % in fluid measured at a center frequency of 680 kHz. The used cantilever has the dimensions of (400 × 140 × 10) μm³.

Keywords: Microcantilever, Fluid-structure interaction, Resonance, Rheology, Eigenfrequency, Adsorption particles.

1. Introduction

The Micro Electromechanical systems (MEMS) use micro-sized components for sensors, transducers, actuators, and electronic. The MEMS appeared in the 1960s, were quickly integrated into electronic products, they appeared with the arrival of microelectronic technologies, and cantilever microbeams are sensors from this MEMS family. The first uses of vibrating cantilevers microbeam for mass detection date back to the 1980s. In 1994, Gimzewski, *et al.* [1] developed a new form of calorimeter based on microcantilever which can sense chemical reaction. In our day, the cantilever microbeams are frequently used to detected biological and chemical microparticles [2-10], to probe viscosity and density of gases and liquids replacing rheometer [11-18] or to detect changes in mass, stress or temperature [19-22]. Wide historical studies have been released on the vibrational microbeam immersed in a fluid [23–25] and many profound theoretical models were done to explain the behavior of the fluid environment and they were ascertained after that by experimental measurements [26-28]. Lately, advanced studies were done by G. Brunetti, *et al.* for the detection of multiple target molecules [29] and with J. Duffy, *et al*. miRNA for the detection of cancer [30] in serum samples.

The process of the system introduces a vibration on the microbeam immersed in a fluid with exciting it periodically by a piezoelectric effect. It is necessary to find the link between the physical parameters of the modification of the natural frequency when the micro-beam is in vibration mode with different surroundings parameters, this linkage helps us in our study. Commonly, two ways of measuring the detection mode are available: by deflection in static mode [31-32] or by shifting resonance in dynamic mode [7, 33].

Generally, many of these applications have been recently developed and used as a very sensitive detector of heat, surface stress, mass or in molecular recognition conducted in a fluid surroundings (gas or liquid). This new model is necessary because it makes progress about detection of gas or humidity in gaseous medium. On the other hand, in liquid medium, they are mainly used for the detection of specific biological molecules (antigen/antibody reactions). The cantilevers microbeam used in the biomedical field are called BioMEMS and this device have become the largest and most diverse applications of MEMS devices. Therefore, it is important to consider how the density of the fluid and the additional mass on the beam affect the behavior of the natural frequency. In other words, measuring the resonant frequency shift during the cantilever excitation frequency sweep reveals an intruder in the surrounding environment.

In our study we will adopt a new method to excite the system by a short electrical pulse periodically on a piezoelectric element embedded in the mass structure of the device, playing the role of an external source (Fig. 1). Then we will try to estimate the variations in the eigenvalue's resonant frequencies. The aim is to prove that with our new proposal we can reach a cantilever system with a beam thickness of 10 µm which will have a high sensitivity compared to other systems.

2. Materials & Methods

Our Methodology begins by using numerical technology and simulating the physical concept with charges effects to illustrate the functional analysis of the results (frequency deviations and electrical signal properties) using a Multiphysics software. Then, the accuracy of the proposed model is validated by close comparison studies of the theoretical calculations to our numerical work using the models of Van Eysden and Sader [34-36].

Several types of excitation are used to make the beam vibrate, the source can be by the effect of electromagnet, thermal noise, or piezoelectric like in our case. Preliminary studies have resulted in the assumption that placing the piezoelectric as a layer under the beam causes the metal to melt at the desired frequencies. Furthermore, this placement also might be causing many reactions with the environment of the experiment since the piezoelectric is in contact with the medium. To avoid these risks, we proposed a new model of structure depicted in Fig. 1, that were the piezoelectric with 10 µm of width is sandwiched in a box of silica. And this box is engraved in an exponential shape ended by a thin beam having a length of 400 µm, width of 140 µm and thickness of 10 µm. This design participates in the transfer of stresses from the box to the beam in an efficient way, by reducing the loss and increasing the quality factor. The maximum frequency of the peak depends on the mass and the rigidity of the structure.

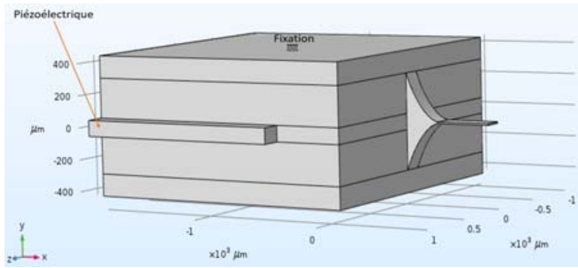

Fig. 1. Mechanical Structure of our device.

A periodic pulse excitation signal is generated by an external source on the piezoelectric while only immersing the beam in a chamber volume of 1.76 µL of incompressible fluid. The maximum displacement of the beam represents the fundamental frequency of the system and creates acoustic pressure on the surrounding fluid as depicted in Fig. 2.

Any change in the resonant frequency for the next pulse is a function of the change in the environmental characteristics, whether it is the mass of viral particles attached to the surface of the cantilever beam or a change in fluid density. Unlike other methods of measurement by optical reflection [3], deflection of the actuated cantilever electrode [37], piezoresistive [38] or shifting in resonance frequency [7], our way of measuring depends on analyzing what can be detected when the voltage pulse goes to 0. A frequency value is read on the piezoelectric, depending on the damping mode caused by the beam that vibrates, in addition to the shifting frequency for two consecutive eigenfrequencies. With this system, installation and nano-wire complicity is reduced. According to a study done by Ghatkesar, *et al*. [39], the peak frequency are notably scattered in function of time as for the eigenfrequencies, they are recorded orderly. These findings drove us to relay on the eigenfrequencies. According to our simulation, the deviation between the peak-frequency and the eigenfrequency is small while increasing in harmonic mode.

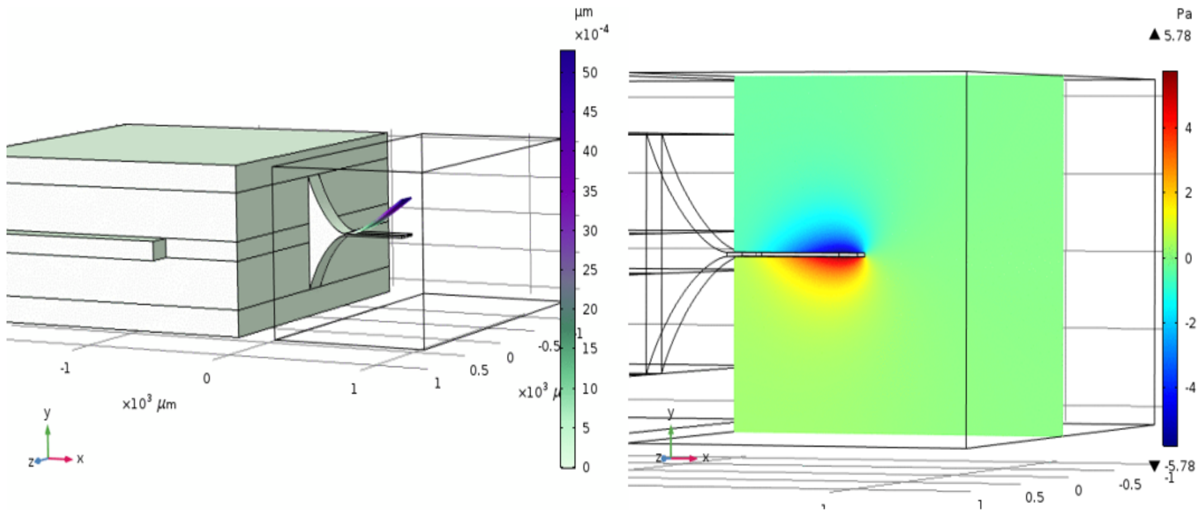

Fig. 2. The displacement of the beam for a fundamental frequency (in the left figure), and the acoustic pressure exerted on the beam by the surrounding for a fundamental frequency (in the right figure).

In these tests, we have found for the order of vibration of the 1st, 2nd, 3rd, 5th and 13th normal mode in a fluid medium in addition to the order vibration of 16th mode in air surrounding, that the beam has an appropriate movement for node fraction, which helps us arriving to the possibility of adsorption on the beam while avoiding the fall of particles from the pores.

3. Results & Discussion

3.1. Density and Dynamic Viscosity Test

The micro-cantilever beam is more sensitive to changes in density than in viscosity while using a beam with 1 µm of width according to Ghatkesar, *et al.* [40].

To move towards greater precision in density and viscosity changes we compared the 5th harmonic mode with the 13th harmonic mode by who have the biggest shift in Eigen frequency while changing in density and viscosity, while using our exponential model, which ends with a beam width of 10 µm. Taking water with 997 kg/m^{-3} of density and 0.913 of viscosity as a reference to examine the frequency changes and to illustrate the sensation variation between our devices of 10 µm of width with other thinner devices. According to our tests done before, as we go up in harmonic mode, there is an increase in the changing frequencies, than with the fluids surrounding tests in this paper, we use the 13th mode as an Eigen value.

The Eigen frequency $\boldsymbol{f_{0n}}$ is characterized by this Eq. (1) in the absence of damping with:

$$f_{0n} = \frac{\alpha_n^2}{2\pi}\sqrt{\frac{k}{3(m_c + m_l)}}, \quad (1)$$

where $\boldsymbol{\alpha_n}$ are related to the different eigenvalues of the harmonics [41], $\boldsymbol{m_c}$ is the mass of cantilever, $\boldsymbol{m_l}$ is the virtual mass of the liquid, $\boldsymbol{k}$ is the spring constant given by $k = 3\frac{EI}{L^3}$, where EI is the flexural rigidity, with E Young's modulus and I the moment of inertia and L is the length of the cantilever. The peak frequency $\boldsymbol{f_n}$ is characterized by this Eq. (2) in the presence of damping with:

$$f_n = \sqrt{f_{0n}^2 \frac{-\gamma^2}{2\pi}}, \quad (2)$$

where the damping factor $\boldsymbol{\gamma}$ is defined by:

$$\gamma = \frac{c_0 + c_v}{\left(\frac{2}{L}\right)(m_c + m_l)}, \quad (3)$$

where $\boldsymbol{c_v}$ is the dissipation coefficient, $\boldsymbol{c_0}$ is the intrinsic damping coefficient per unit length that describes internal losses.

In 5 % of glycerol test and 5 % of ethylene glycol test we inferred that the viscosity is constant, per contra in 5 % of glycerol test and 12 % of ethylene glycol the density is constant. These tests in Fig. 3 are carried out to make a comparison between the density and the viscosity at the level of frequency sensitivity.

As we can see in the Fig. 3, in 5 % of glycerol, the numerical eigenfrequencies shifted in the center of 680 kHz by −2690 Hz, in 12 % of ethylene glycol, it shifted by −2910 Hz and in 5 % of ethylene glycol, it shifted by −1260 Hz.

Correspondingly, in 5 % of glycerol, the analytical eigenfrequencies shifted in the 13th mode by −4178 Hz, in 12 % of ethylene glycol, it shifted by −4514.6 Hz and in 5 % of ethylene glycol, it shifted by −1833.8 Hz.

We have noticed that the change in density is 0.055 % and the change in viscosity is 4.41 %.

Our findings suggest that the beam thickness used with this model has better density sensitivity than previous models.

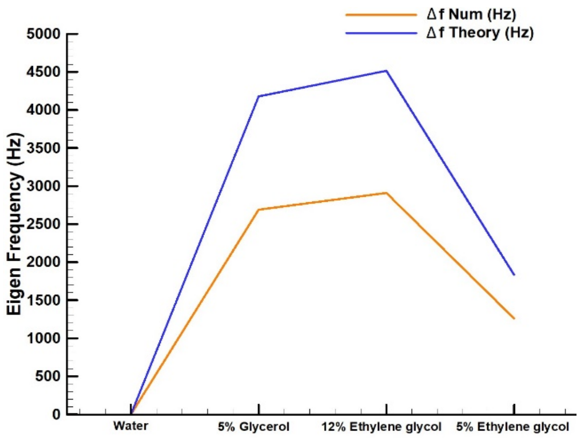

Fig. 3. Theoretical and numerical shifts Eigen frequency were calculated according to [35] at mode 13^{th}.

3.2. Adsorption Particles

Potassium is a chemical element that exists in the form of an ion in the body. It is present in the serum and too much or too little potassium in the blood plasma can lead to cardiac complications. The normal value of the potassium level should be between 3.5 and 5 mmol/L, of all human beings. A decrease in potassium levels called "hypokalemia"(<3.5 mmol/L) often caused by digestive problems, can cause fatigue, muscle cramps [42]. Too much potassium in the blood is called "hyperkalemia"(>4.5 mmol/L) and can cause serious heart problems, which can lead to cardiac arrest and death without emergency chelation therapy. Several studies on the cardiac disease are done to detect a specific marker in serum the C-reactive protein for this pathology [3]. In fact, our model is based on the density variation caused by the potassium rate. The potassium level in mmol/L can affect the serum density in kg/m³ according to this equation $\boldsymbol{Cm}=\boldsymbol{CM}\times\boldsymbol{MM}$ where $\boldsymbol{Cm}$ is mass concentration in g/L, $\boldsymbol{CM}$ is molar concentration in mol/L and $\boldsymbol{MM}$ is the potassium molar mass, equals to 39.1 g/mol.

We took a serum density of 1024.136 kg/m³ as an arbitrary value for a normal patient as an example, who have an Eigen frequency between 640510 Hz and 640530 Hz.

The density increases while increasing the amount of potassium and decreases while decreasing the amount of potassium as shown in Table 1. The frequency shift is from 640510 Hz to 640460 Hz with 0.254 g/L of density for hyperkalemia disease (>5 mmol/L) and from 640530 Hz to 640400 Hz with -0.136 g/L of density for hypokalemia disease (<3 mmol/L) insofar as shown in Fig. 4. We have noticed that the change is 20 Hz/mmol.L^{-1}.

Table 1. Showing the effect of potassium rate (in mmol/L and g/L) on the liquid density, and displaying the variation in density with that of the frequency in the13^{th} mode.

Total Density Kg/m³	1024.0	1024.039	1024.078	1024.117	1024.136	1024.176	1 024.19	1 024.23	1 024.27	1 024.31	1 024.35	1 024.39
Potassium Rate g/L	0	0.039	0.078	0.117	0.136	0.176	0.19	0.23	0.27	0.31	0.35	0.39
Potassium Rate mmol /L	0	1	2	3	3.5	4.5	5	6	7	8	9	10
Mode 13th Hz	640600	640580	640560	640540	640530	640510	640500	640490	640490	640480	640470	640460

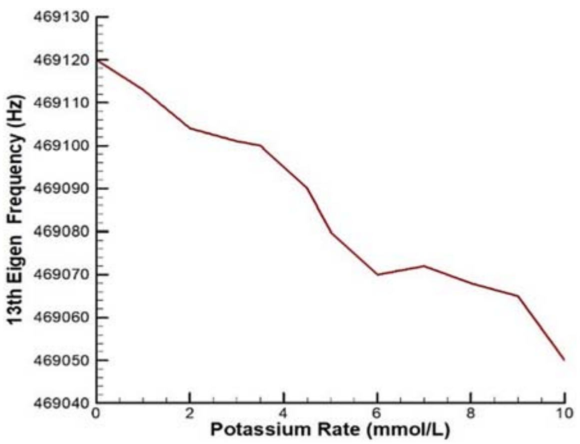

Fig. 4. Variation of the 13^{th} natural frequency mode with the potassium level and indicate the range of the patient hypokalemia, normal and hyperkalemia.

By examining the curve shown in Fig. 4, it can be noticed that the change in frequency is shifted by 140 Hz in a change of 0.39 g/L of potassium. Moreover, the SiO_2 is a porous material where the average pore diameter is between 2.6 and 68.3 nm [43] compatible with the diameter of potassium particles of 550 pm. Based on the aforementioned, it is possible that these potassium beads are adsorbed on the beam during the vibration, and this will be a great incentive to change the Eigen frequency.

The validation was done using COMSOL Multiphysics software as depicted in Fig. 5 with the red beads being the potassium particles and the bleu lines being the beam clamped on one edge. The change in the Eigen frequency as a function of the mass of particles attached to the surface of the cantilever beam constitutes could be the basis of the detection scheme.

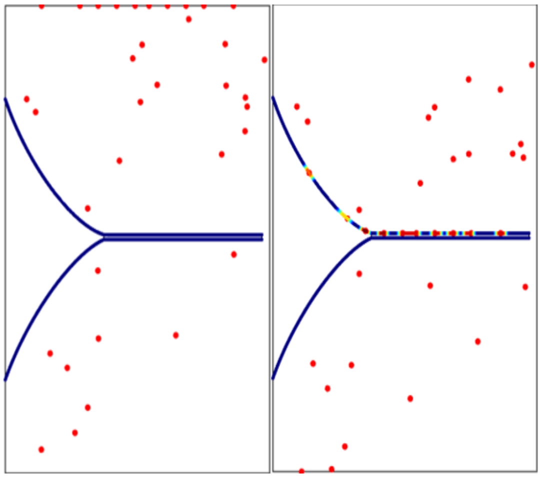

Fig. 5. Potassium adsorption on the surface of SiO_2 beam.

3.3. Added Mass

For an additional optimization, we made several numerical estimations of Δf variation for two different methods of added masses on the beam as shown in Fig. 6.

For the accuracy, this test is validated by a close comparison of the studies of the theoretical calculations with our numerical works by using this equation:

$$f_{0n} = \frac{\alpha_n^2}{2\Pi}\sqrt{\frac{k}{3(m_c + m_l + \Delta m)}}, \quad (4)$$

where $\boldsymbol{\Delta m}$ is related to the loaded mass distributed on the surface of the cantilever and the eigen frequency $\boldsymbol{f_{0n}}$ is characterized by this Eq. (4) in the absence of damping.

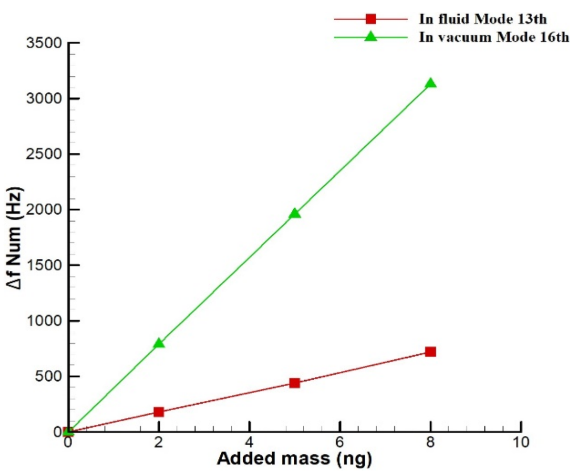

Fig. 6. Δf Num in fluid for Mode13th and in vacuum for Mode 16th.

As shown in Fig. 6, the first test was at the center of 640 kHz (13th Mode) surrounded by a fluid and the mass was added on the whole surface with an accuracy of 90 Hz/ng. The second test was at the center of 961 kHz (16th Mode) under vacuum and the mass was added on the whole surface with an accuracy of 390 Hz/ng.

Our numbers show that in liquid medium the shifting frequency is much more pronounced than in vacuum owing to the influence of hydrodynamic force on the cantilever.

4. Conclusions & Outlook

According to our findings, this new microcantilevers shape have been designed to analyze their sensitivity in a chosen medium and it has proven effective. This device can detect up to 0.055 % density and 4.4 % viscosity changes, measured in a chamber volume of 1.76 μL in mode 13th. Consequently, it can diagnose the patient's disease based on the frequency change caused by the potassium level present in the serum by a precision of 20 Hz/mmol.L^{-1}. Furthermore, this device can detect a small added mass in vacuum by an accuracy of 390 Hz/ng with mode 16th and in fluid by an accuracy if 90 Hz/ng with mode 13th. However, we should ascertain our data with the experimental part using physical realization by laser engraving on SiO_2 support and integrating the excitation source in the overall structure. Then we should verify these values by the analytical part.

The target in this study is to pave the way for several biological topics and especially the diseases that have signs in the blood and urine. Detecting cancer before it metastasizes by the detection of trace biological entities in the serum, can save a patient, prevent disease progress, and give possibility of diagnosing the pathology at its very first stage before spreading. Our future goal is to develop a system with arrays of eight silica beam for the early detection of cancerous potential, it makes it possible to identify new genetic and epigenetic biomarkers linked to any cancer present in the blood, and to find a specific coated cantilever for each disease. This paper could be interesting for several research where we can use the analyzing natural frequency shift as a sign for a disease by studying the rheological serum properties.

References

[1]. J. K. Gimzewski, Ch. Gerber, E. Meyer, R. R. Schlittler, Observation of a chemical reaction using a micromechanical sensor, *Chemical Physics Letters*, Vol. 217, Issue 5, January. 1994, pp. 589-594.

[2]. H. Lang, *et al.*, A chemical sensor based on a micromechanical cantilever array for the identification of gases and vapors, *Applied Physics A*, Vol. 66, 1998, pp. S61-S64.

[3]. C.-H. Chen, *et al.*, A Wireless Bio-MEMS Sensor for C-Reactive Protein Detection Based on Nanomechanics, *IEEE Transactions on Biomedical Engineering*, Vol. 56, Issue 2, 2009, pp. 462-470.

[4]. I. Dufour, D. Rebiere, F. Lochon, Détection de COV: des microcapteurs à base de micropoutres, *InfoChimie Magazine*, Vol. 468, January 2006, pp. 66-69.
[5]. F. Huber, H. Lang, N. Backmann, D. Rimoldi, C. Gerber, Direct detection of a BRAF mutation in total RNA from melanoma cells using cantilever arrays, *Nature Nanotechnology*, Vol. 8, 2013.
[6]. K. Hwang, Jeong Hoon Lee, J. Park, D. Yoon, J. Park, T. Kim, In-situ quantitative analysis of a prostate-specific antigen (PSA) using a nanomechanical PZT cantilever, *Lab on a Chip*, Vol. 4, January 2005, pp. 547-52.
[7]. J. H. Lee, K. S. Hwang, J. Park, K. H. Yoon, D. S. Yoon, T. S. Kim, Immunoassay of prostate-specific antigen (PSA) using resonant frequency shift of piezoelectric nanomechanical microcantilever, *Biosensors and Bioelectronics*, Vol. 20, Issue 10, 2005, pp. 2157-2162.
[8]. X. Zhou, S. Wu, H. Liu, X. Wu, Q. Zhang, Nanomechanical label-free detection of aflatoxin B1 using a microcantilever, *Sensors and Actuators B: Chemical*, Vol. 226, November 2015, pp. 24-29.
[9]. W. Zhou, A. Khaliq, Y. Tang, H. Ji, R. R. Selmic, Simulation and design of piezoelectric microcantilever chemical sensors, *Sensors and Actuators A: Physical*, Vol. 125, Issue 1, Oct. 2005, pp. 69-75.
[10]. A. Gupta, D. Akin, R. Bashir, Single virus particle mass detection using microresonators with nanoscale thickness, *Appl. Phys. Lett.*, Vol. 84, Issue 11, 2004, pp. 1976-1978.
[11]. N. Belmiloud, I. Dufour, L. Nicu, A. Colin, J. Pistre, Vibrating Microcantilever used as Viscometer and Microrheometer, Preprint in 2006 *IEEE SENSORS*, Oct. 2006, pp. 753-756.
[12]. W. Shih, X. Li, H. Gu, W.-H. Shih, I. Aksay, Simultaneous liquid viscosity and density determination with piezoelectric unimorph cantilevers, *Journal of Applied Physics*, Vol. 89, Issue 2, 2001.
[13]. N. Belmiloud, I. Dufour, A. Colin, L. Nicu, Rheological behavior probed by vibrating microcantilevers, *Appl. Phys. Lett.*, Vol. 92, Issue 4, 2008, p. 041907.
[14]. S. Boskovic, J. W. M. Chon, P. Mulvaney, J. E. Sader, Rheological measurements using microcantilevers, *Journal of Rheology*, Vol. 46, Issue 4, 2002, pp. 891-899.
[15]. D. Kim, S. Hong, J. Jang, J. Park, Determination of Fluid Density and Viscosity by Analyzing Flexural Wave Propagations on the Vibrating Micro-Cantilever, *Sensors*, Vol. 17, Issue 11, 2017, p. 2466.
[16]. M. Youssry, N. Belmiloud, B. Caillard, C. Ayela, C. Pellet, I. Dufour, A straightforward determination of fluid viscosity and density using microcantilevers: Analytical and experimental studies, *Procedia Engineering*, Vol. 5, 2010, pp. 1035-1038.
[17]. M. Hennemeyer, S. Burghardt, R. W. Stark, Cantilever Micro-rheometer for the Characterization of Sugar Solutions, *Sensors*, Vol. 8, Issue 1, January 2008, pp. 10-22.
[18]. A. Quist, A. Chand, S. Ramachandran, D. Cohen, R. Lal, Piezoresistive cantilever based nanoflow and viscosity sensor for microchannels, *Lab Chip*, Vol. 6, Issue 11, 2006, pp. 1450-1454.
[19]. M. Toda, N. Inomata, T. Ono, I. Voiculescu, Cantilever beam temperature sensors for biological applications, *IEEJ Transactions on Electrical and Electronic Engineering*, Vol. 12, Issue 2, 2017, pp. 153-160.
[20]. N. V. Lavrik, M. J. Sepaniak, P. G. Datskos, Cantilever transducers as a platform for chemical and biological sensors, *Review of Scientific Instruments*, Vol. 75, Issue 7, 2004, pp. 2229-2253.
[21]. I. Voiculescu, F. Liu, T. Ono, M. Toda, Investigation of bimaterial cantilever beam for heat sensing in liquid, *Sensors and Actuators A: Physical*, Vol. 242, 2016, pp. 58-66.
[22]. T. Thundat, R. J. Warmack, G. Y. Chen, D. P. Allison, Thermal and ambient□induced deflections of scanning force microscope cantilevers, *Appl. Phys. Lett*., Vol. 64, Issue 21, 1994, pp. 2894-2896.
[23]. J. E. Sader, Frequency response of cantilever beams immersed in viscous fluids with applications to the atomic force microscope, *Journal of Applied Physics*, Vol. 84, Issue 1, 1998, pp. 64-76.
[24]. R. Berger, Ch. Gerber, H. P. Lang, J. K. Gimzewski, Micromechanics: A toolbox for femtoscale science: “Towards a laboratory on a tip”, *Microelectronic Engineering*, Vol. 35, Issue 1, 1997, pp. 373-379.
[25]. C.-C. Liang, C.-C. Liao, Y.-S. Tai, W.-H. Lai, The free vibration analysis of submerged cantilever plates, *Ocean Engineering*, Vol. 28, Issue 9, September 2001, pp. 1225-1245.
[26]. W. Lin, N. Qiao, Vibration and stability of an axially moving beam immersed in fluid, *International Journal of Solids and Structures*, Vol. 45, Issue 5, 2008, pp. 1445-1457.
[27]. M. Aureli, M. Porfiri, Low frequency and large amplitude oscillations of cantilevers in viscous fluids, *Appl. Phys. Lett.*, Vol. 96, Issue 16, 2010, p. 164102.
[28]. E. Grimaldi, M. Porfiri, L. Soria, Finite amplitude vibrations of a sharp-edged beam immersed in a viscous fluid near a solid surface, *Journal of Applied Physics*, Vol. 112, Issue 10, November 2012, p. 104907.
[29]. G. Brunetti, *et al*., Nanotechnological immunoassay for rapid label-free analysis of candidate malaria vaccines, *Nanoscale*, Vol. 13, 2021, pp. 2338-2349.
[30]. J. Duffy, F. Padovani, G. Brunetti, P. Noy, U. Certa, M. Hegner, Towards personalised rapid label free miRNA detection for cancer and liver injury diagnostics in cell lysates and blood based samples, *Nanoscale*, Vol. 10, 2018.
[31]. G. Thakur, K. Jiang, D. Lee, K. Prashanthi, S. Kim, T. Thundat, Investigation of pH-Induced Protein Conformation Changes by Nanomechanical Deflection, *Langmuir*, Vol. 30, Issue 8, 2014, pp. 2109-2116.
[32]. K. Jiang, *et al*., Rapid and Highly Sensitive Detection of Dopamine Using Conjugated Oxaborole-Based Polymer and Glycopolymer Systems, *ACS Appl. Mater. Interfaces*, Vol. 9, Issue 18, 2017, pp. 15225-15231.
[33]. J. Joo, D. Kwon, C. Yim, S. Jeon, Highly Sensitive Diagnostic Assay for the Detection of Protein Biomarkers Using Microresonators and Multifunctional Nanoparticles, ACS Nano, Vol. 6, 2012, pp. 4375-4381.
[34]. C. A. Van Eysden, E. Sader, Resonant frequencies of a rectangular cantilever beam immersed in a fluid, *Journal of Applied Physics*, Vol. 100, Issue 11, 2006, p. 114916.
[35]. C. A. Van Eysden, J. E. Sader, Frequency response of cantilever beams immersed in viscous fluids with applications to the atomic force microscope: Arbitrary mode order, *Journal of Applied Physics*, Vol. 101, Issue 4, 2007, p. 044908.

[36]. C. A. Van Eysden, J. E. Sader, Frequency response of cantilever beams immersed in compressible fluids with applications to the atomic force microscope, *Journal of Applied Physics*, Vol. 106, Issue 9, 2009, p. 094904.

[37]. M. SoltanRezaee, M. Bodaghi, Simulation of an electrically actuated cantilever as a novel biosensor, *Scientific Reports*, Vol. 10, Issue 1, 2020, 3385.

[38]. K. W. Wee, *et al.*, Novel electrical detection of label-free disease marker proteins using piezoresistive self-sensing micro-cantilevers, *Biosensors and Bioelectronics*, Vol. 20, Issue 10, 2005, pp. 1932-1938.

[39]. T. Braun, *et al.*, Micromechanical mass sensors for biomolecular detection in a physiological environment, *Physical Review E, Statistical, Nonlinear, and Soft Matter Physics*, Vol. 72, 2005, p. 031907.

[40]. M. K. Ghatkesar, E. Rakhmatullina, H.-P. Lang, C. Gerber, M. Hegner, T. Braun, Multi-parameter microcantilever sensor for comprehensive characterization of Newtonian fluids, *Sensors and Actuators B: Chemical*, Vol. 135, Issue 1, 2008, pp. 133-138.

[41]. P. A. A. Laura, J. L. Pombo, E. A. Susemihl, A note on the vibrations of a clamped-free beam with a mass at the free end, *Journal of Sound and Vibration*, Vol. 37, Issue 2, Nov. 1974, pp. 161-168.

[42]. Potassium: comprendre son taux lors d'une prise de sang. https://sante.journaldesfemmes.fr/fiches-anatomie-et-examens/2493150-potassium-comprendre-taux-prise-de-sang/ (consulté le mai 17, 2021).

[43]. T. Mochizuki, D. Atong, S.-Y. Chen, M. Toba, Y. Yoshimura, Effect of SiO_2 pore size on catalytic fast pyrolysis of Jatropha residues by using pyrolyzer-GC/MS, *Catalysis Communications*, Vol. 36, 2013, pp. 1-4.

Sensors & Transducers
Published by IFSA Publishing, S. L., 2021
http://www.sensorsportal.com

Anisotropy of Attenuation of Acoustic Waves in Lanthanum Gallosilicate Crystals

[1] Farkhad Akhmedzhanov, [1] Temur Mustafaev and [2] Jamoliddin Nazarov
[1] Institute of Ion-Plasma and Laser Technologies, 33 Durmon Yuli str., 100125 Tashkent, Uzbekistan
[2] Navoi State Mine Institute, 27a Yuzhnaya str., 210100, Navoi, Uzbekistan
Tel.: + 998-902121998, fax: + 998-712623183
E-mail: akhmedzhanov.f@gmail.com

Received: 9 November 2021 /Accepted: 13 December 2021 /Published: 30 December 2021

Abstract: Anisotropy of the attenuation of acoustic waves in lanthanum gallosilicate crystals have been studied by the Bragg light diffraction method in the frequency range from 0.4 to 1.6 GHz. The results were used to determine the real and imaginary elastic constants for these crystals, which can be used to construct the acoustic attenuation surfaces. It is shown that lanthanum gallosilicate crystals are characterized by relatively high anisotropy of attenuation coefficient of acoustic waves. The observed effect is explained by the strong dependence of the effective Grüneisen constant on the direction of the wave vector.

Keywords: Acoustic wave, Anisotropy of attenuation, Gruneisen constant, Lanthanum gallosilicate crystals, Real and imaginary elastic constants, Bragg diffraction method.

1. Introduction

The main material for creating sensors operating on the piezoelectric effect is thermostable and high-Q quartz, on which resonators are created in a wide frequency range from hundreds of hertz to 100 MHz. However, significant disadvantages of quartz are the relatively low value of the electromechanical coupling coefficient and the phase transition at a temperature of 573 ºC with the loss of piezoelectric properties [1].

Crystals of tantalate and lithium niobate are strong piezoelectrics, characterized by high thermal and chemical stability, but also have a phase transition at temperatures of 620 ºC and 1145 ºC, respectively. In addition, these crystals have a pyroelectric effect, due to which an electrical signal in the crystal arises not only from external pressure, but also from temperature [2, 3].

Compared to these materials used in sensors of physical quantities, single crystals of the langasite family have a number of advantages: thermal stability of piezoelectric characteristics, no pyroelectric effect, and no phase transitions up to a melting temperature of 1470 °C [4-7]. The effectiveness of the use of these crystals is associated with a high coefficient of electromechanical coupling that is 3-4 times higher than the coefficient of electromechanical coupling of quartz.

A well-known representative of this family is lanthanum hallosilicate crystals ($La_3Ga_5SiO_{14}$), which significantly exceeds quartz in piezoelectric coefficients, has thermostable cuts for bulk and surface acoustic waves, and is of great interest for modern acoustics, acoustoelectronics, and piezotechnics [7, 8].

One of the parameters limiting the use of crystals in acoustics and acoustoelectronics is the acoustic attenuation coefficient. The main mechanism of attenuation of acoustic waves in the region $\omega\tau \ll 1$ (ω is the circular frequency of the acoustic wave, τ is the relaxation time of thermal phonons) is the Akhiezer mechanism [9, 10]. This mechanism of acoustic attenuation is assumed that the frequency of acoustic wave is below that of any possible relaxations in the crystal. If the thermal phonon relaxation times are short with the period of acoustic waves, then the complex elastic tensor can be used to describe the loss of acoustic wave's energy [9, 11].

The real components of the complex elastic tensor are known for great number crystals [1, 4]). At the same time the imaginary components, describing attenuation of acoustic waves, were not practically investigated. The most detailed researches of imaginary components of elastic tensor have been made in [11-14].

For a complete description of the anisotropy of the acoustic properties of crystals, along with the characteristic surfaces of the propagation velocity of acoustic waves, it is convenient to use the acoustic attenuation surfaces. This approach was first proposed in the study of the anisotropy of acoustic attenuation in crystals of magnesium oxide [11] and lithium niobate [12] and was used in this work to analyze the anisotropy of attenuation of longitudinal and transverse acoustic waves in lanthanum hallosilicate crystals.

2. Samples and Experimental Method

Samples were prepared in the form of a cube with length of edges 12 mm. The faces of the cube have been oriented with accuracy no worse than 1° along the crystallographic axes [001], [100] and [010] or [001], [110] and [1-10], respectively. To excite longitudinal or transverse acoustic waves, lithium niobate plate transducers (X or rotated Y-cut) were used, which had a thickness of 40 or 70 μm.

The velocity and attenuation of acoustic waves were investigated with the help of Bragg diffraction of light on acoustic waves in the frequency range 0.4–1.2 GHz at room temperature [15]. The measurements were carried out using an acousto-optic setup consisting of a system for exciting acoustic waves and a system for recording diffracted laser light (wavelength 632.8 nm). The helium-neon laser with a wavelength of 632.8 nm was used as a light source. The intensities of diffracted light were measured with the help of photoelectric multiplier.

The acoustic wave velocity V was determined from the Bragg diffraction angle with the accuracy of 0.2 % [1]:

$$V = \lambda\nu / 2\sin\theta_B , \quad (1)$$

where ν is the linear frequency of acoustic wave, θ_B is the external Bragg angle.

The attenuation coefficient was calculated with the accuracy ~ 5 % by the formula [15]:

$$\alpha = 10\lg\left(I_1/I_2\right) / 2L_0 \quad (2)$$

Here L_0 is the length of the sample, I_1 and I_2 are respectively the intensity of the light diffracted on the direct acoustic wave and the intensity of the light diffracted on the wave, reflected from the free end of the sample, at the same point along the direction of propagation of acoustic waves. The corresponding distances and time intervals between the indicated signals were also measured.

The Formula (2) is easily derived from consideration of the dependence of the measured values of light intensities on the distance along the direction of propagation of the acoustic wave.

3. Results and Discussion

The experimentally obtained values of velocity and attenuation of longitudinal and transverse acoustic waves along the crystallographic directions [100], [010] and [001] in LGS crystals are shown at Table 1. In this table $\boldsymbol{q}$ and $\boldsymbol{\gamma}$ are the directions of wave vector and polarization vector, respectively.

Table 1. Velocity and acoustic attenuation in LGS crystals (ν= 1 GHz, T = 293 K).

q	γ	V, 10^3 m s^{-1}	α, dB·μs^{-1}
[100]	[1 0 0]	5.73	0.20
	[0 0.83 -0.56]	2.39	0.35
	[0 0.56 0.83]	3.32	0.23
[010]	[0 0.996 -0.092]	5.75	0.21
	[0 0.092 0.996]	3.02	0.31
	[1 0 0]	2.71	0.28
[001]	[0 0 1]	6.75	0.15
	[1 0 0]	3.06	0.31

The measurement results given in the Table 1 make it possible to determine first the effective values of the real and imaginary elastic constants for the studied directions of propagation of acoustic waves, which, in turn, can be represented as a certain combination of the elastic tensor components [11]:

$$c'_{eff} = c'_{ijkl}\kappa_j\kappa_l\gamma_i\gamma_k , \quad (3)$$

$$c''_{eff} = c''_{ijkl}\kappa_j\kappa_l\gamma_i\gamma_k , \quad (4)$$

where κ_j and γ_i are the components of the unit wave normal $\boldsymbol{\kappa}$ and the polarization vector $\boldsymbol{\gamma}$, respectively. c'_{ijkl} and c''_{ijkl} are the real and imaginary components of the complex tensor of elastic constants:

$$c_{ijkl} = c'_{ijkl} + ic''_{ijkl} \quad (5)$$

It should be noted that some of the effective values of the elastic constants are equal to one of the components of the corresponding part of the elastic tensor, which facilitates their determination.

For example, for longitudinal waves propagating along the [100] direction, the following relations are valid:

$$c'_{eff} = c'_{11}, \tag{6}$$

$$c''_{eff} = c''_{11} \tag{7}$$

In the same way, for longitudinal waves propagating along the [001] direction, the following relations are valid:

$$c'_{eff} = c'_{33}, \tag{8}$$

$$c''_{eff} = c''_{33} \tag{9}$$

Symmetry properties and, accordingly, the number of independent components of the imaginary part of the elastic tensor are the same as for the real part, which is used to analyze the orientation dependence of the phase and group velocities of acoustic waves in crystals [1, 6].

For lanthanum gallosilicate crystals (point symmetry group 32), from the experimental data on the velocity and attenuation of acoustic waves, along with seven real elastic coefficients, seven independent components of the imaginary part of the elastic coefficient tensor should be determined (in the matrix notation: c''_{11}, c''_{12} c''_{13}, c''_{14}, c''_{33}, c''_{44}, c''_{66}).

The area of our research satisfies the condition ωτ<<1, where ω is the frequency of acoustic wave, τ is relaxation time of thermal phonons. The acoustic attenuation in this region can be expressed in terms of the real and the imaginary part of the complex elastic constants [11]:

$$\alpha = \frac{1}{2}\omega\frac{c''_{eff}}{c'_{eff}} \tag{10}$$

Expressions (3) and (4) can be written in terms of the real and imaginary components of the Green–Christoffel tensors, which are the convolution of the material tensor of elastic constants respectively real or imaginary, over the direction cosines of the wave vector [11, 14].

In particular, the imaginary effective values of elastic constants are determined by expression

$$c''_{eff} = \Gamma''_{ik}\gamma_i\gamma_k = \frac{2\alpha\rho V^2}{\omega}, \tag{11}$$

where ρ is the density of crystal.

Using Eq. (11), it is possible to determine the attenuation coefficient of acoustic waves in a crystal for any directions of the wave vector. These directions are included in the expressions for the effective elastic constants c'_{eff} (3) and c''_{eff} (4). It can be seen that the general form of these expressions is determined by the symmetry of the crystal and the direction cosines of the unit wave normal and the polarization vector.

The experimental results were used to calculate all the independent real and imaginary components of the complex tensor of elastic constants, with the help of which it is possible to determine the characteristics of acoustic waves along any arbitrary direction in crystal. It should be noticed that the obtained real elastic constants are in good coincidence with data from [5].

As a result we used the next real elastic constants:

c'_{11}=18.8·10^{10} Н/м^2, c'_{33} =26.2·10^{10} Н/м^2,

c'_{44}=5.37·10^{10} Н/м^2, c'_{66} =4.21·10^{10} Н/м^2,

c'_{13}=9.69·10^{10} Н/м^2, c'_{14} =1.41·10^{10} Н/м^2.

The accuracy of determining these real constants of the elasticity tensor was approximately 1 %.

The corresponding imaginary components of the elastic tensor were also calculated:

c''_{11}=2.78·10^6 Н/м^2, c''_{33} =2.90·10^6 Н/м^2,

c''_{44}=1.23·10^6 Н/м^2, c''_{66} =0.95·10^6 Н/м^2,

c''_{13}=0.26·10^6 Н/м^2, c''_{14} =-0.52 10^6 Н/м^2.

The accuracy of determining the imaginary constants of the elasticity tensor was worse due to the relatively large error in determining the attenuation coefficients of acoustic waves and amounted to about 10 %.

We considered the anisotropy of velocity and attenuation of all three modes of acoustic waves during their propagation in the crystallographic plane (100), orthogonal to the second-order symmetry axis. In this case, the direction cosines are κ_1=0, κ_2=cosφ, κ_3=sinφ.

The anisotropy of the propagation velocity of longitudinal and transvers acoustic waves in the (100) plane is shown in Fig. 1. It is seen, that the largest change in velocity by a factor of 1.4 is observed for pure transverse waves in this plane. While for other waves the change in the velocity value does not exceed 20 % for quasi-longitudinal waves and 16 % for quasi-shear waves.

It should be noted that in the investigated plane (100) there are two acoustic axes, one of which coincides with the symmetry axis of the third order [001] and the other is directed at an angle of 42 degrees to the Y axis. Transverse waves propagating along this acoustic axis are pure, since as the polarization vector of one of them is directed perpendicular to the (100) plane, and the polarization vector of the second transverse wave deflected by 90 degrees relative to the direction of the wave vector in the same plane.

The imaginary components of the Green-Christoffel tensor can be are written as:

$$\Gamma''_{11} = c''_{66}\cos^2\varphi + c''_{44}\sin^2\varphi + 2c''_{14}\sin\varphi\cos\varphi, \tag{12}$$

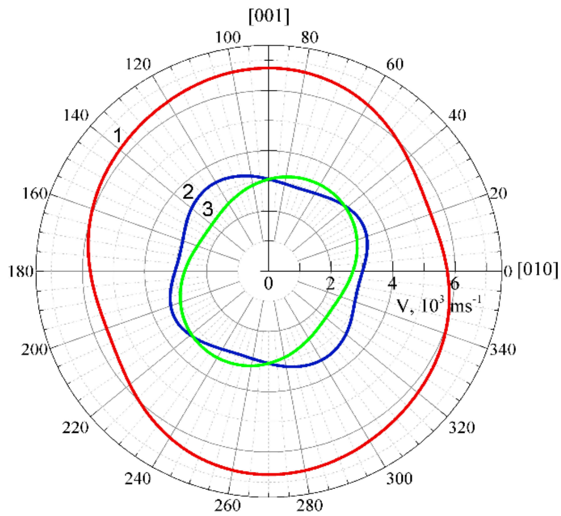

Fig. 1. Cross-section of the surface of the velocity of quasilongitudinal (1), quasi-transverse (2) and transverse acoustic waves (3) in $La_3Ga_5SiO_{14}$ crystals by the plane (100).

$$\Gamma''_{22} = c''_{11}\cos^2\varphi + c''_{44}\sin^2\varphi - 2c''_{14}\sin\varphi\cos\varphi, \quad (13)$$

$$\Gamma''_{33} = c''_{44}\cos^2\varphi + c''_{33}\sin^2\varphi, \quad (14)$$

$$\Gamma''_{23} = \Gamma''_{32} = (c''_{13} + c''_{44})\sin\varphi\cos\varphi - c''_{14}\cos^2\varphi, \quad (15)$$

$$\Gamma''_{12} = \Gamma''_{21} = \Gamma''_{13} = \Gamma''_{31} = 0 \quad (16)$$

As a result, the imaginary part of the effective elastic constant for acoustic waves, the polarization of which lies in the plane of their propagation (100), is determined by the expression [8]:

$$c''_{eff} = \frac{1}{2}\left(\Gamma''_{22} + \Gamma''_{33}\right) \pm \frac{1}{2}\sqrt{(\Gamma''_{22} - \Gamma''_{33})^2 + 4\Gamma''_{23}} \quad (17)$$

Note that in order to determine the real part of the effective elastic constant c'_{eff}, it is necessary to replace the imaginary components with real ones in equation (12). The imaginary part of the effective elastic constant for the pure transverse acoustic wave, the polarization of which is perpendicular to the plane (100), is equal $c''_{eff} = \Gamma''_{11}$ and changes with the direction in this plane according to Eq. (12).

First of all, our studies have shown that the attenuation of high-frequency acoustic waves in langasite is noticeably greater than in quartz, which is possibly due to the disordered structure of these crystals due to the deficiency of Ga + and Si + ions arising directly during their growth. According to [7], the introduction of TiO_2 and Al_2O_3 oxides into lanthanum hallosilicate crystals promotes the filling of the corresponding positions in the lattice with Al^{3+} and Ti^{4+} ions intended for Ga^{3+} and Si^{4+} ions, while the structure of the LGS+Al and LGS+Ti crystals becomes ordered and relaxation losses are reduced.

The anisotropy of the attenuation coefficients of longitudinal and transverse acoustic waves in the form of a cross-section of the attenuation surface by the plane (100) is shown in Fig. 2.

It is seen that lanthanum gallosilicate crystals are characterized by relatively high anisotropy of attenuation coefficient of acoustic waves. Especially it is true for pure transverse acoustic waves in examined plane. For these waves in the (100) plane, the maximum attenuation coefficient differs from the minimum attenuation by almost six times. For quasi-longitudinal and quasi-transverse acoustic waves, the ratio of the maximum attenuation value to the minimum value is approximately two.

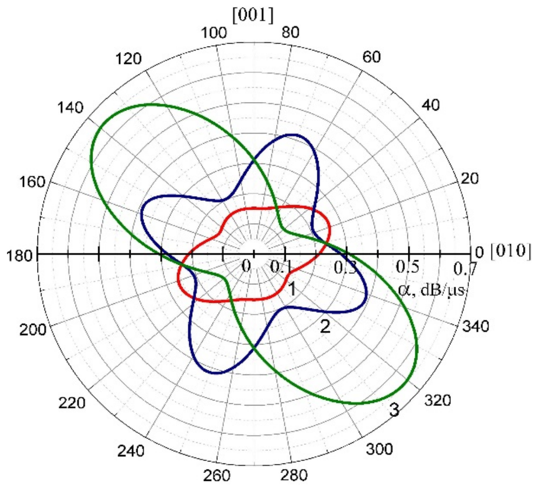

Fig. 2. Cross-section of the attenuation surface of quasilongitudinal (1), quasi-transverse (2) and transverse acoustic waves (3) by the plane ZOY in $La_3Ga_5SiO_{14}$ crystals.

The results of our investigations showed also that, in lanthanum hallosilicate crystals, there is no relationship between the velocity anisotropy and the attenuation anisotropy of acoustic waves. Although, according to Expression (10), the attenuation anisotropy is determined by the anisotropy of both real and imaginary effective elastic constants.

At the same time, there is a clear connection between the anisotropy of attenuation and the anisotropy of the imaginary part of the effective elastic constant. Fig. 3 shows the orientation dependence of three quantities in relative units, including the real effective elastic constant, the imaginary effective elastic constant and the attenuation coefficient for longitudinal acoustic waves in the crystallographic plane (100).

It can be seen that the anisotropy of the acoustic attenuation coefficient almost completely coincides with the orientation dependence of the imaginary effective elastic constant.

The observed regularity is well explained by the fact that the anisotropy of acoustic attenuation is primarily due to the dependence of the Gruneisen anharmonicity constant on the direction of the wave vector of the acoustic wave [9, 10, 14]. This constant enters into the expression determining the value of the attenuation coefficient of acoustic waves by the Akhiezer mechanism [9, 10] and, according to Eq. (11), determines also the orientation dependence of the imaginary part of the effective elastic constant.

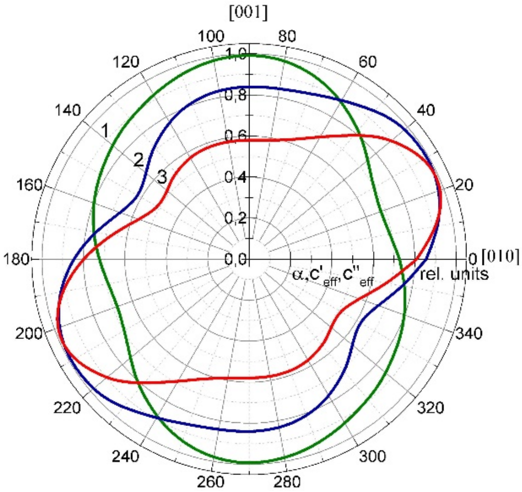

Fig. 3. Orientation dependence of the real effective elastic constant (1), the imaginary effective elastic constant (2), and the attenuation coefficient (3) for longitudinal acoustic waves in the plane (100).

4. Conclusions

Our studies have shown that the cavities of the attenuation coefficient of quasi-transverse and pure transverse waves intersect in two directions, one of which at an angle of about 10 degrees to the [010] axis in the (100) plane does not coincide with the direction of the acoustic axis, known from studies of the transverse wave velocities in lanthanum hallosilicate crystals. And this interesting result requires further detailed study of the propagation of transverse acoustic waves in other planes of symmetry.

The obtained results on the anisotropy of acoustic attenuation in LGS crystals will be useful in the development of acoustic and acoustoelectronic devices, including sensors and piezoelectric resonators based on lanthanum hallosilicate crystals.

References

[1]. E. Dieulesaint, D. Royer, Elastic waves in solids, Application for treatment of signals, *Nauka*, Moscow, 1982.

[2]. Andrushchak A. S., Mytsyk B. G., Laba H. P., *et al.*, Complete sets of elastic constants and photoelastic coefficients of pure and MgO-doped lithium niobate crystals at room temperature, *Journal of Applied Physics*, Vol. 106, 2009, pp. 073510-1 – 073510-6.

[3]. Chezganov D. S., Shur V. Ya., Baturin I. S., Akhmatkhanov A. R., *et al.*, Polarization reversal in crystals of congruent lithium tantalate at elevated temperatures, *Ferroelectrics*, Vol. 439, Issue 1, 2012, pp. 40-46.

[4]. Andreev I. A., Single crystals of the langasite family: An intriguing combination of properties promising for acoustoelectronics, *Technical Physics*, Vol. 51, Issue 6, 2006, pp. 758-764.

[5]. Sotnikov A. V., Kunze R., Schmidt H., Weihnacht M., Hengst M., Gotze J., Piezoelectric and elastic properties of $Sr_3NbGa_3Si_2O_{14}$ (SNGS) single crystals, *Physics of the Solid State*, Vol. 51, Issue 2, 2009, pp. 275-279.

[6]. Kazantsev S. G., Ovcharenko T. N., Calculated and experimental study of the anisotropy of elastic properties of piezoelectric single crystals of the langasite group, *Electromechanics*, Vol. 123, 2011, pp. 51-59.

[7]. I. A. Andreev, Anisotropy and dispersion of the velocity and absorption of elastic waves in piezoelectric crystals, *Experimental Physics*, Issue 6, 2015, pp. 27-43.

[8]. F. R. Akhmedzhanov, T. Sh. Mustafaev, J. T. Nazarov, Attenuation of Acoustic Waves in Langasite Crystals, in *Proceedings of the 3rd IFSA Frequency & Time Conference (IFTC '2021)*, Palma de Mallorca, Mallorca, Spain, 22-24 September 2021, pp. 40-43.

[9]. Yu. A. Logachev, B. Ya. Moyzhes, On the theory of sound absorption according to Akhizer, *Solid State Physics*, Vol. 16, Issue 8, 1974, pp. 2219-2223.

[10]. R. Nava, M. P. Vecchi, J. Romero, B. Fernandez, Akhiezer damping and the thermal conductivity of pure and impure dielectrics, *Phys. Rev. B.*, Vol. 14, Issue 2, 1976, pp. 800-807.

[11]. F. R. Akhmedzhanov, V. V. Lemanov, A. Nasyrov, Surfaces of acoustic attenuation in crystals, *Letters Journal Technical Physics (SU)*, Vol. 6, Issue 10, 1980, pp. 589-592.

[12]. I. L. Bajak, A. McNab, J. Richter, C. D. Wilkinson, Attenuation of acoustic waves in lithium niobate, *J. Acoust. Soc. Am.*, Vol. 69, Issue 3, 1981, pp. 689-695.

[13]. Wenhua Jiang, Wenwu Cao, High-frequency dispersion of ultrasonic velocity and attenuation of single crystal 0.72 $Pb(Mg_{1/3}Nb_{2/3})O_3$ – 0.28 $PbTiO_3$ with engineered domain structures, *Appl. Phys. Lett.*, Vol. 80, 2002, pp. 2466-2468.

[14]. F. R. Akhmedzhanov, S. Z. Mirzaev, U. A. Saidvaliev, Parameters of Elastic Anisotropy in Bismuth Silicate Crystals, *Ferroelectrics*, Vol. 556, Issue 01, 2020, pp. 23-28.

[15]. F. R. Akhmedzhanov, J. O. Kurbanov, A. F. Boltabaev, Attenuation of Acoustic Waves in Single-domain and Polydomain $LiTaO_3$ Crystals, *Sensors & Transducers*, Vol. 246, Issue 7, 2020, pp. 43-47.

Sensors & Transducers, Vol. 254, Issue 7, December 2021, pp. 43-46

Sensors & Transducers
Published by IFSA Publishing, S. L., 2021
http://www.sensorsportal.com

Anisotropy of Acoustooptical Properties of Lithium Niobate Crystals

F. R. Akhmedzhanov, U. Sh. Abdirakhmonov and V. N. Avdievich
Institute of Ion-Plasma and Laser Technologies, TMS Laboratory, 33 Durmon Yuli str., 100125 Tashkent, Uzbekistan
Tel.: + 998-902121998, fax: + 998-712623183
E-mail: akhmedzhanov.f@gmail.com

Received: 19 November 2021 /Accepted: 20 December 2021 /Published: 30 December 2021

Abstract: Anisotropy of acoustooptical properties of lithium niobate crystals has been studied, when the direction of the light wave vector changes in the plane perpendicular to the direction of propagation of the acoustic wave. The values of components of the photoelastic tensor were determined by the Dixon method. It is shown that for the main geometries of Bragg diffraction of light, when acoustic waves propagate along the crystallographic axes, the acousto-optical quality factor is approximately the same for both longitudinal and transverse acoustic waves. The results obtained on the anisotropy of acousto-optical interaction in lithium niobate crystals can be useful for their application in acousto-optical devices for measuring the frequency of acoustic waves based on the phenomenon of acoustical activity.

Keywords: Acousto-optical quality factor, Photoelastic constants, Acoustic waves, $LiNbO_3$ crystals, Dixon method.

1. Introduction

The study of the anisotropy of acoustooptical properties of crystals is quite important for determining the most effective crystal cuts used as working media and optimizing the parameters of acousto-optic devices.

As shown in [1], even within the Pockels model, finding the extreme directions in a crystal that provide the maximum value of the effective photoelastic constant requires solving a system of 21 nonlinear fourth, third, and second order equations with high rank tensors. In this regard, the photoelastic properties of crystals are usually considered for specific geometries of acousto-optic interaction and for certain cuts of the crystal [2].

In the literature, as a rule, most works are devoted to determining the acousto-optical quality factor M_2, which was introduced by Dixon [3] as a characteristic of the efficiency of Bragg diffraction at acoustic waves and determines the intensity of diffracted light in a given material, regardless of the size of the piezoelectric transducer and the power of the acoustic wave:

$$M_2 = \frac{n_1^3 n_2^3 p_{эфф}^2}{\rho V^3}, \tag{1}$$

where n_1 and n_2 are the refractive indices of the incident and diffracted light, respectively, ρ is the density, V is the velocity of the acoustic wave.

The effective photoelastic constant, p_{eff} in relation (1) is the convolution of the values of components of the photoelastic tensor p_{ijkl} of the crystal with respect to the normalized polarization vectors, respectively, of the diffracted and incident light α and β, and the direction and polarization of the acoustic wave κ and γ [1, 3]:

$$p_{эфф} = p_{ijkl}\alpha_i\beta_j\gamma_k\kappa_l \tag{2}$$

Thus, the coefficient M_2 depends on the geometry of the diffraction of light by sound and makes it possible to assess the acousto-optic properties of materials. By changing the direction of the polarization of the incident light relative to the wave vector and the polarization of the acoustic wave, one can influence the value of the effective photoelastic constant and, ultimately, control the efficiency of Bragg diffraction of light in this crystal. Such experiments also make it possible to identify the most optimal geometries of Bragg diffraction for obtaining the highest intensity of diffracted light.

In the present work, the anisotropy of effective photoelastic constants and the acousto-optical quality factor M_2 in lithium niobate crystals, which are widely used in different acousto-optic devices [3], has been investigated. Despite the fact that the components of the photoelastic tensor of these crystals have been determined in many works, the anisotropy of the effective photoelastic constants has not been fully investigated, and there are also inaccuracies in the available works [5–8].

2. Samples and Experimental Technics

Cylindrical lithium niobate samples with a length of about 15 mm and a diameter of 6 mm were oriented along the directions [100], [010] and [00]) with an accuracy of no worse than 1 degree. The surfaces of the samples were processed and polished with optical precision.

The measurements were carried out by the Bragg light diffraction method [1, 3]. Piezoelectric quartz plates (X or Y-cut) were used to excite longitudinal or transverse acoustic waves with frequencies of 400–1200 MHz. The helium-neon laser with a wavelength of 632.8 nm was used as a light source. The intensities of diffracted light were measured with the help of photoelectric multiplier.

To determine the effective photoelastic constants, a modified Dixon-Cohen method was used, in which acoustic waves are excited both from the side of the standard specimen and from the side of the studied sample [7]. Upon excitation of acoustic waves from the side of the standard specimen, the values of the intensity of light diffracted in the standard specimen I_{1st} and the studied sample I_{1x} were measured.

Then, acoustic waves were excited from the side of the studied sample, and the light intensities in the sample I_{2x} and the standard specimen I_{2st} were measured again. A sample of fused silica was used as the standard specimen. The acoustic contact of the sample with the samples was carried out using epoxy resin.

The values of the effective photoelastic constants for different geometries of the Bragg diffraction of light were determined from the relation:

$$\left[\frac{p_{eff}^2 n^6}{\rho V^3}\frac{n^2}{(n+1)^4}\right]_x = \left[\frac{p_{eff}^2 n^6}{\rho V^3}\frac{n^2}{(n+1)^4}\right]_{st}\left(\frac{I_{1x}I_{2x}}{I_{1st}I_{2st}}\right)^{\frac{1}{2}}, \qquad (3)$$

where ρ is the density of the crystal; n is the refractive index of light; V is the velocity of the acoustic wave.

The values of the velocity of acoustic waves required for the calculation were determined from the angle of Bragg diffraction of light at these waves with an accuracy of about 0.2%. The values of the remaining quantities required for the calculation were taken from [8, 9]. The accuracy of determining the effective photoelastic constants was approximately 15 %.

3. Results and Discussion

One of the universal methods for studying the elastic and photoelastic properties of materials, including piezoelectric and ferroelectric crystals, are acousto-optic methods based on the Bragg diffraction of light by acoustic waves [1, 4]. In this case, the intensity of the diffracted light is determined by the effective photoelastic constant p_{eff}, the value of which can be obtained using the transformation formulas for the components of the fourth-rank tensor [1, 2]. Using simple transformations, one can obtain an expression for determining the effective photoelastic constants in the form:

$$p^2_{эфф}=(\chi_1 P_2-\chi_2 P_1)^2+(\chi_1 P_3-\chi_3 P_1)^2+(\chi_2 P_3-\chi_3 P_2)^2 \qquad (4)$$

where χ_j are the direction cosines of the wave vector of the diffracted light, P_i are the values of the light polarization components, which are calculated by the formula:

$$P_i=p_{iklm}\cdot\beta_k\cdot\gamma_l\cdot\kappa_m, \qquad (5)$$

where p_{iklm} are the components of the photoelastic tensor, β_k are the direction cosines of the polarization of the incident light, γ_l and κ_m are the direction cosines of the polarization and the wave vector of the acoustic wave respectively.

The experimentally obtained values of the effective photoelastic constants were used to determine the components of the photoelastic tensor in lithium niobate crystals using relations (3) and (4). The expressions for the effective photoelastic constants (in terms of the components of the photoelastic tensor p_{ijkl}) for some geometries of Bragg light diffraction in lithium niobate crystals are presented in Table 1. In this table $\boldsymbol{q}$ is the wave vector of acoustic wave, $\boldsymbol{\gamma}$ is the polarization of the acoustic wave, $\boldsymbol{k}$ is the wave vector of the light and $\boldsymbol{\beta}$ is the unit vector of polarization of the light incident on the sample.

It can be seen that for many geometries of Bragg diffraction, the effective photoelastic constant is equal to one of the components of the photoelastic tensor, that facilitates their determination.

As a result the next absolute values of photoelastic constants have been obtained:
p_{11}=0.031, p_{33}=0.086, p_{44}=0.046, p_{66}=0,024, p_{12}=0.081, p_{13}=0.090. p_{14}=0.075, p_{31}=0.175, p_{41}=0.156.

The accuracy of determining these constants of the photoelasticity tensor was approximately 15 %. It is worth noting the relatively high value of the photoelastic constant p_{44} that allows one to expect a high intensity of light diffracted on the transverse acoustic waves in lithium niobate crystals.

Table 1. Expressions p_{eff} for some geometries of Bragg light diffraction in lithium niobate crystals.

q	γ	k	β	$P_{eff.}$
[001]	Z	arbitr.	$\parallel$ q	p_{33}
			$\perp$ q	p_{13}
	X	X	arbitr	0
		Y	arbitr	p_{44}
		k^X=α	$\parallel$ q	$p_{44}\mathrm{Sin}\alpha$
			$\perp$ q	$(p_{14}^2\sin^2 2\alpha + p_{44}^2\sin^2\alpha)^{1/2}$
[100]	X	Z	$\perp$ q	p_{12}
		Y	$\perp$ q	p_{31}
		k^Z=α	$\perp$ q	$p_{12}\cos^2\alpha+p_{31}\sin^2\alpha +p_{41}\sin 2\alpha$
	γ^Z =φ	Z	arbitr	$p_{14}\cos\varphi+p_{66}\sin\varphi$
		Y	arbitr	$P_{41}\sin\varphi+P_{44}\cos\varphi$

Based on the values of the components of the photoelastic tensor determined by the Dixon method, the anisotropy of the effective photoelastic constants p_{eff} in these crystals has been studied for the case of propagation of longitudinal acoustic waves along the [100] direction and transverse acoustic waves along the [001] direction, when the light is incident and diffracted in the crystallographic plane perpendicular (accurate to the Bragg angle) to the wave vector q of the acoustic wave under an arbitrary angle.

The cross section of the surface of the square of the effective photoelastic constant by the (100) plane for Bragg light diffraction on the transverse acoustic waves in $LiNbO_3$ crystals is presented at Fig. 1. The direction of the light polarization is perpendicular to the direction of propagation of acoustic wave. It is seen that for transverse waves along the [001] direction, the effective photoelastic constant varies from zero to the maximum value when the wave vector of light is directed approximately along the [110] axis.

The calculations according to the expression from Table 1 showed that the square of the effective photoelastic constant for light Bragg diffraction by transverse waves propagating along the 001 axis reaches its maximum value (0.0066 10^{-15} s^3/kg) when the light is incident at an angle of 47 degrees to the [100] axis in the (001) plane. This direction is the most effective for acousto-optical interaction of light with transverse acoustic waves along the [001] axis.

Similar anisotropy was investigated for isotropic diffraction of light by longitudinal acoustic waves along the [100] direction, when the diffraction occurs without rotation of the plane of the light polarization.

The geometry of this Bragg diffraction is described by the equation:

$$p_{eff}=p_{12}\cos^2\alpha+p_{31}\sin^2\alpha \qquad (6)$$

The direction of the incident light was changed in the (100) plane. The results of calculation are shown in Fig. 2.

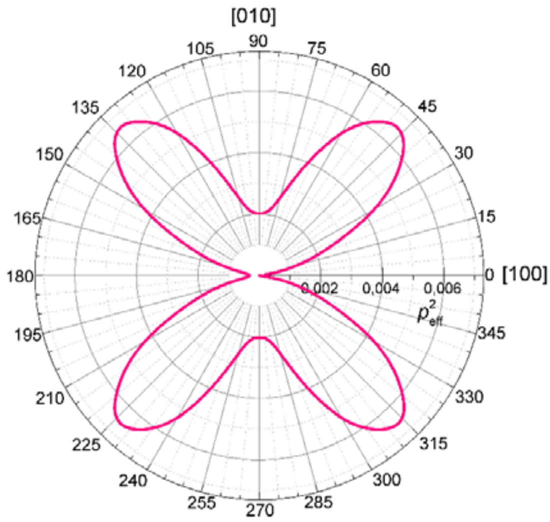

Fig. 1. Anisotropy of the square of the effective photoelastic constant in $LiNbO_3$ crystals for transverse waves along [001] at different orientation of the light wave vector in the plane (001).

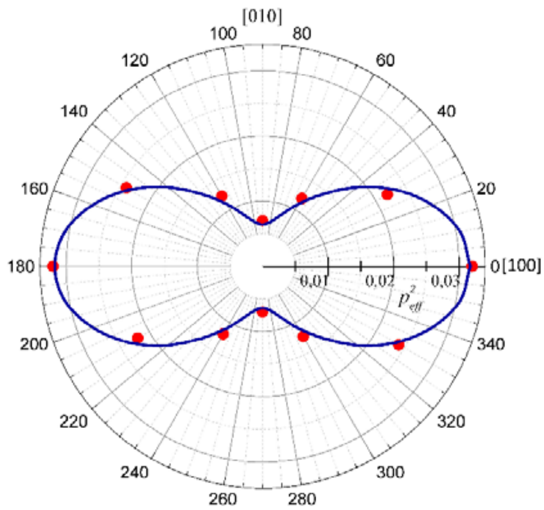

Fig. 2. Anisotropy of the square of the effective photoelastic constant in $LiNbO_3$ crystals for longitudinal waves along [100] at different orientation of the light wave vector in the plane (100). Points are results of the experiment.

Simultaneously, measurements were carried out to determine the intensity of the diffracted light, which, as is known, is proportional to the square of the effective photoelastic constant. The direction of the wave vector of light incident perpendicularly (accurate to the Bragg angle) on the lateral surface of the sample was changed by rotating the sample around the direction of propagation of the longitudinal acoustic wave with a step of 30 degrees. The direction of polarization of the light incident on the sample, relative to the wave vector and the polarization of the acoustic wave was determined using a polarization analyzer.

The results of the measurements (in the form of points) are also shown in Fig. 2. Intensity values are given in relative units. The maximum value was taken to be the intensity of the light diffracted along the [010] direction. It is seen that the experimental results are in good agreement with the calculated dependence.

It should be noted that, in the general case, the effective photoelastic constant for anisotropic Bragg diffraction by longitudinal acoustic waves propagating along the [100] axis is described by a more complex dependence, the expression of which is given in Table 1.

In this case, the maximum intensity of diffracted light in the specified geometry of Bragg diffraction will be observed when the light propagates at a certain angle to the [010] axis in the (100) plane. This angle can be determined by the photoelastic constants p_{12}, p_{31}, and p_{41}.

The calculations of the acousto-optical quality factor were carried out for some of the most commonly used light diffraction geometries, which are given by the directions, respectively, of the wave vectors of sound $\boldsymbol{q}$ and light $\boldsymbol{k}$, and the polarization of sound $\boldsymbol{\gamma}$ and incident light $\boldsymbol{\beta}$. Cases were considered when longitudinal and transverse acoustic waves propagate along the [100] and [001] directions.

The calculation results are shown in Table 2, in which the values of the attenuation coefficient of these waves at a frequency of 1 GHz are also given [11].

It can be seen that for the considered geometries of Bragg diffraction of light, the acousto-optical quality coefficient is approximately the same for both longitudinal and transverse acoustic waves. Thus, the geometry of acousto-optic interaction shown in Fig. 1 can be successfully applied to study the acoustic activity in lithium niobate crystals [10].

Table 2. Acousto-optical quality factor M_2 for some geometries of Bragg light diffraction in lithium niobate crystals.

q	**γ**	**β**	**k**	α, dB/μs	M_2, 10^{-15} s^3/kg
[001]	[001]	[010]	[100]	0.12	6.6
[001]	[001]	[001]	[100]	0.12	4.5
[001]	⊥[001]	[001]	[110]	0.25	4.7
[100]	[100]	[010]	[001]	0.28	5.4
[100]	⊥[001]	[100]	[001]	0.24	1.6

It should be noted that some of the obtained values of the coefficient M_2 are in good agreement with the results in [1, 2].

4. Conc1usions

The calculation results were shown that the square of the effective photoelastic constant in lithium niobate crystals for longitudinal waves along the [100] axis has a relatively large value of ~ 0.03. At the same time, as can be seen from the results of this study, this constant for transverse waves is an order of magnitude lower than for longitudinal waves.

The results obtained on the anisotropy of acousto-optical interaction in lithium niobate crystals can be useful for their application in acousto-optical devices for measuring the frequency of acoustic waves based on the phenomenon of acoustical activity. In particular, one can choose the most optimal geometry of Bragg diffraction of light by transverse acoustic waves in lithium niobate crystals.

References

[1]. E. Dieulesaint, D. Royer, Elastic waves in solids. Application for treatment of signals, *Nauka*, Moscow, 1982.

[2]. R. W. Dixon, Acousto-optic interaction and devices. *IEEE Trans*, V. ED-17, No 1, 1980, pp. 229-235.

[3]. R. S. Weis, T. K. Gaylord. Lithium Niobate: Summary of physical properties and crystal structure, *J. Appl. Phys.*, Vol. A37. 1985, pp. 191-196.

[4]. A. S. Andrushchak, B. G. Mytsyk, H. P. Laba, *at. el.*, Complete sets of elastic constants and photoelastic coefficients of pure and MgO-doped lithium niobate crystals at room temperature, *J. Appl. Phys,* Vol. 106, 2009, pp. 073510 (1-6).

[5]. M. Jazbinsek and M. Zgonik, Material tensor parameters of LiNbO3 relevant for electro- and elasto-optics, *J. Appl. Phys.,* Vol. B74, 2002, pp. 407-412.

[6]. A. Erba, R. Dovesi, Photoelasticity of crystals from theoretical simulations, *Phys. Rev*., Vol. B88, 2013, pp. 045121.

[7]. R. W. Dixon, M. G. Cohen, A new technique for measuring magnitudes of Photoelastic Tensors and its Application to Lithium Niobate, *Appl. Phys. Letter*, Vol. 8, 1966, pp. 205-207.

[8]. V. M. Petrov, A. V. Shamray, Microwave integrated optical modulators. Theory and practice, *ITMO University*, St. Petersburg, 2021.

[9]. Acoustic crystals, Ed. M. P. Shaskolskaya, *Nauka*, Moscow, 1982.

[10]. F. R. Akhmedzhanov, Application of acoustical activity for measurement of acoustic wave frequency, in *Proceedings of the Frequency Control Symposium, joint with the 22nd European Frequency & Time Forum*, Besancon, France, 2009, pp. 613-615.

[11]. F. R. Akhmedzhanov, F. N. Juraev, Attenuation of Acoustic Waves in Lithium Niobate Crystals with Impurities, in *Proceedings of the International Conference on Acoustics 2012,* Nantes, France, April 23-27, 2012, 000801.

5th International Conference on Optics, Photonics and Lasers (OPAL' 2022)

18-20 May 2022

Tenerife (Canary Islands), Spain

http://www.opal-conference.com

About the Event

Similar to the previous OPAL conferences, the 5th International Conference on Optics, Photonics and Lasers (OPAL' 2022) will incorporate three symposiums covering a broaden range in optics, photonics and lasers, and provide an excellent opportunity to exchange ideas and present latest advancements in these areas. The OPAL 2022 will be organized by the IFSA - a professional, non-profit association serving for industry and academy for 20 years.

The purpose of OPAL' 2022 is bring together leading international researchers, engineers and practitioners interested on any of the optical related technologies. The conference will offer plenary and invited talks, contributed oral and poster presentations, special sessions, tutorials, and exhibitions of commercial products. Social and cultural events will also take place to foster networking among the participants in a friendly manner.

Optics:

- Optical and Fibre Optical Sensors and Instrumentation
- Micro-Opto-Electro-Mechanical Systems (MOEMS)
- Physical Optics
- Optoelectronic Devices, Photonics, Nanophotonics and Biophotonics
- Organic Optoelectronics and Integrated Photonics
- Optical Communications, Switching and Networks
- High-speed Opto-electronic Networking
- Optical Fiber Technology: Materials, Devices and Systems
- Optical Information Processing
- Holography
- Optical Metrology
- Optical Imaging Systems and Machine Vision
- Optical Computing
- Guided Wave Optics
- Optics in Condensed and Soft Matter
- Quantum Optics
- Lasers and Laser Applications
- Nonlinear Optics
- Nano and Micro Optics
- Matter Waves
- Quantum Information
- Bio and Medical Optics
- Optical Materials, Characterization Methods and Techniques
- Optical Methods for Process Control
- Microscopy and Adaptive Optics
- Lasers in Medicine and Biology
- Engineering Applications of Spectroscopy
- Optical Microscopy of Composites

Photonics:

- Photonic Sensors
- Photodetectors
- Photonic Integrated Circuit (PIC)
- Photonic Integration and Packaging
- Photonic Crystals
- Biophotonics
- Microwave Photonics
- Nanophotonics
- Photonic Materials and Metameterials
- Quantum Photonics
- Terahertz Photonics
- Photonic Computing
- Applications of Photonic Technologies

Lasers:

- Laser Science
- Laser and laser optics
- Semiconductor Lasers
- Laser Metrology
- Chemical Gas Lasers
- Fiber Lasers
- Nonlinear Lasers
- Laser Propulsion
- Lasers and LEDs
- Laser Nanotechnology
- Laser Spectroscopy and Microscopy
- Laser Applications
- Lasers in Medicine and Biology

5^{th} International Conference on Optics, Photonics and Lasers (OPAL' 2022)

2022 OPAL

Deadlines:

Submission (2-page abstract):	5 March 2022
Notification of acceptance:	20 March 2022
Registration:	5 April 2022
Camera ready (4-6 pages paper):	15 April 2022

One event - three publications !

1) All registered abstracts will be published in the conference proceedings (USB flash drive edition of published Proceedings with the ISBN), distributed during the conference and submitted for indexing to the Web of Science. The previous OPAL' 2018 - 2021 Conference proceedings were indexed by the Conference Proceedings Citation Index.

THOMSON REUTERS CONFERENCE PROCEEDINGS CITATION INDEX INDEXED

2) Authors will be invited to submit full-page extended papers to the special issue of Sensors & Transducers open access journal (ISSN 2306-8515, e-ISSN 1726-5479) for free of charge.

3) The limited number of full-page papers published in the journal will be selected by the Editorial Board to extend for book chapters for the open access Book Series on 'Advances in Optics: Reviews', Vol. 6.

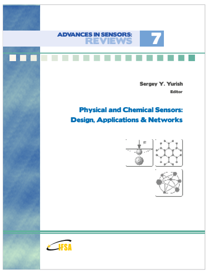

Social Programme

Welcome Cocktail: The Welcome Cocktail will take place on the 16^{th} floor (Sky Lounge Bar) situate on the Hard Rock Hotel's Nirvana Tower building's roof with the best, magnificent, panoramic views to Teide volcano, the Atlantic coast, La Gomera Island and sunset. Actually, it is known as the highest leisure location in Tenerife. Do not miss this opportunity to say the first "hello" to attendees and committee members.

Gala Dinner: The Gala Dinner (BBQ) will take place in the Hard Rock Hotel at the sea beach in front of the Lagoon area.

Contribution Types:

- Keynote presentations
- Invited talks
- Special sessions
- Regular sessions
- Poster session
- Industrial presentations
- Exhibition
- Round tables

Special Sessions:

Participants are welcome to organize and manage special sessions during the conference. Each session will contain 4-6 papers in a related field as specified above.

Session organizers will get:

- Certificate of Appreciation
- Free Registration for the Event
- Special Publishing Theme within Conference Proceedings
- Free article and book chapter post conference publications in appropriate open access journals and 'Advances in Optics: Reviews', Book Series, Vol. 6

Organising Committee

Chairman:
Prof., Dr. Sergey Y. Yurish (IFSA, Spain)

Advisory Chairmen:
Dr. Qiang Wu
(Northumbria University, Newcastle Upon Tyne, UK)
Prof., Dr. Claude Phipps (Photonic Associates, USA)
Prof., Dr. George Semouchkin
(Michigan Technological University, USA)
Prof., Dr. Sandeep Singh Sengar
(University of Copenhagen, Denmark)
Prof., Dr. Boris Mizaikoff (Ulm University, Germany)
Prof., Dr. Mahmoud Daoudi
(National Center for Nuclear Sciences and Technologies, Tunisia)

Conference Manager:
Mrs. Tetyana Zakharchenko
(IFSA Publishing, S.L., Spain)

IFSA Publishing IOP Institute of Physics physicsworld

Call for Chapters

IFSA Publishing

Your Chapter may be in the next Volume of the popular Book Series

ADVANCES IN SENSORS: REVIEWS 8

Open Access Book Series

Sinse 2012

- Physical, chemical and biosensors
- Sensor uncertainty, accuracy, calibration
- Smart sensors and systems
- Intelligent sensors and systems
- Artificial Intelligence enabled sensors
- Virtual and soft sensors
- Sensor instrumentation
- Sensor buses and networks
- Signal processing, sensor fusion
- Nanosensors
- Photonic sensors
- Sensor interfacing and signal conditioning
- Materials for sensors
- MEMS, BioMEMS and NEMS
- Remote Sensors and Telemetry
- Sensor packages and reliability

https://www.sensorsportal.com/HTML/IFSA_Publishing.htm

IFSA

International Frequency Sensor Association Publishing

www.sensorsportal.com

ISSN 1726- 5479

9 771726 547001